Applied Mathematical Modelling 150 (2026) 116324

Contents lists available at ScienceDirect

Applied Mathematical Modelling

journal homepage: www.elsevier.com/locate/apm

A simple approach for effective CFD simulation of turbulent pipe transport of shear-thinning, power-law fluids

J.I. Soto [a,b,*], G.V. Messa [b], M.R. Malin [c], W. Brevis [a]

[a] Departamento de Ingeniería Hidráulica y Ambiental, Pontificia Universidad Católica de Chile, Av. Vicuña Mackenna 4860, 7820426, Santiago, Chile

[b] Dipartamento di Ingegnieria Civile e Ambientale, Politecnico di Milano, Piazza Leonardo da Vinci 32, 20133, Milano, Italy

[c] Concentration Heat and Momentum Limited (CHAM), Bakery House, 40 High Street Wimbledon Village, SW19 5AU, London, United Kingdom

ARTICLE INFO

Keywords:
Shear-thinning
Power-law
Turbulent flow
Pipe-flow
CFD
Low-Reynolds number turbulence model

ABSTRACT

This study presents a simple, efficient approach for the CFD simulation of turbulent pipe transport of shear-thinning, power-law fluids. The method is developed within the Newtonian-based Reynolds-Averaged Navier-Stokes (RANS) framework, and it relies on a modification to the Reynolds-averaged apparent viscosity function to compensate for errors induced by the non-decomposition of the instantaneous apparent viscosity, as well as for the use of turbulence models developed for Newtonian fluids. Specifically, the Reynolds-averaged apparent viscosity switches from a power law to a logarithmic function for averaged shear rates below a threshold value, called the "critical shear rate", which becomes a calibration parameter of the model. The new framework was tested against DNS data reported in the literature for different pipe-flow conditions, covering combinations of flow index $n = \{1.0, 0.8, 0.6\}$ and friction Reynolds number $\mathrm{Re}_\tau = \{323, 500, 750\}$, as well as against well-established correlations for the friction factor, with the analysis extended to cases up to $n = 0.4$ and $\mathrm{Re}_\tau = 2,500$. The analysis was conducted by employing three different turbulence models, namely Lam-Bremhorst k-ε, two-layer k-ε, and k-ω SST, which all rely on a low-Reynolds number treatment to obtain a detailed flow description in the near-wall region. The proposed approach appears attractive from an engineering standpoint, as it allows obtaining reasonably accurate prediction of main features of turbulent pipe transport of shear-thinning, power-law fluids, with a simple mathematical formulation and a robust and easy-to-converge character that can make a difference for the application to more complex flows.

1. Introduction

Many industrial processes involve pipeline transport of non-Newtonian fluids. For instance, the transport of non-settling slurries in the mining industry, i.e., waste materials comprising fine particles homogeneously distributed and strongly coupled with the carrier liquid can be modelled as pseudo-fluids with non-Newtonian properties [1]. Other examples of transportation of non-Newtonian fluids includes concentrated domestic slurries [2] and fresh concrete [3]. Depending on the solid particle concentration, these materials exhibit varying degrees of shear-thinning viscosity and solid-like behaviour characterised by yield stress, but generally show low elasticity, i.e., limited elastic recovery after deformation. As such, they can be classified as purely viscous non-Newtonian fluids.

* Corresponding author at: Departamento de Ingeniería Hidráulica y Ambiental, Pontificia Universidad Católica de Chile, Av. Vicuña Mackenna 4860, 7820426, Santiago, Chile.

E-mail address: jisoto8@uc.cl (J.I. Soto).

https://doi.org/10.1016/j.apm.2025.116324
Received 29 January 2025; Received in revised form 14 July 2025; Accepted 16 July 2025

Available online 24 July 2025

In a purely viscous non-Newtonian fluid, the deviatoric component of the stresses tensor τ_{ij} is a nonlinear function of the apparent viscosity μ. The typical constitutive model is shown in Eq. (1):

$$\tau_{ij} = 2\mu(\dot{\gamma})s_{ij}, \quad s_{ij} = \frac{1}{2}\left(\frac{\partial u_i}{\partial x_j} + \frac{\partial u_j}{\partial x_i}\right) \tag{1}$$

where the shear rate $\dot{\gamma} = (2s_{ij}s_{ij})^{1/2}$ is the second invariant of the deformation rate tensor s_{ij}, the velocity vector is u_i, and the position vector (in Cartesian coordinates system) is x_i. Depending on the function relating the apparent viscosity to the shear rate, we might have different non-Newtonian fluids. In the mining industry, the simplest model to represent the non-Newtonian behaviour of a slurry is the power-law model [4]:

$$\mu = m\dot{\gamma}^{n-1} \tag{2}$$

The model parameters m and n are denominated consistency and flow index, respectively. When $0 < n < 1$, which is the case of interest in this research, the fluid is shear-thinning, and the apparent viscosity decreases when the shear rate is increased. Conversely, when $n > 1$, the flow is shear thickening, and the apparent viscosity increases with increasing the shear-rate. Eq. (2) reduces to the Newtonian fluid model when $n = 1$, and the apparent viscosity becomes equal to the constant m, representing the molecular viscosity of Newtonian fluids.

The power-law rheology model is widely used due to its simplicity and its ability to provide a good approximation of viscosity in many industrial applications [5,6]. However, caution is needed when applying this model at very low shear rates, since many other materials, such as polymer solutions, exhibit a constant viscosity in the zero-shear-rate region, whereas the shear-thinning power-law model inaccurately predicts infinite viscosity. This limitation becomes less relevant in turbulent flows, where high-shear-rate rheological data are more critical for accurately characterizing the flow dynamics. In the context of fully developed turbulent pipe flow, it is recommended to obtain rheological data at shear rates at least twice those associated with the mean wall shear stress [7]. Under such conditions, the choice of a more complex model than the power-law, such as the Herschel-Bulkley model which accounts for yield stress at low shear rates, has limited influence on the predicted flow behaviour [7]. This should remain valid when the yield stress is much smaller than the wall shear stress, thereby preventing the formation of unyielded, solid-like regions in the flow core as observed in simulations of turbulent flows [8,9]. Based on these considerations, and in view of the numerical challenges associated with implementing more complex constitutive models, we restrict our analysis to purely viscous non-Newtonian fluids described by the power-law model.

When introducing the constitutive model of a non-Newtonian fluids into the momentum conservation equations, a generalized formulation of the Navier-Stokes (NS) equations is obtained:

$$\frac{\partial u_i}{\partial x_i} = 0 \tag{3a}$$

$$\rho\frac{\partial u_i}{\partial t} + \rho u_j\frac{\partial u_i}{\partial x_j} = -\frac{\partial p}{\partial x_i} + \frac{\partial}{\partial x_j}\left[\mu(\dot{\gamma})\left(\frac{\partial u_i}{\partial x_j} + \frac{\partial u_j}{\partial x_i}\right)\right] + \rho g_i \tag{3b}$$

where p is the pressure, ρ is the fluid density and g_i is the body force per unit of mass. However, significant challenges arise when simulating the transport of non-Newtonian fluids in the turbulent regime. One possibility would be to directly solve for the instantaneous generalized NS equations, which would be analogous to the Direct Numerical Simulation (DNS) in Newtonian fluids. Given the technical challenges of experimental testing, simulations of this type are basically the only viable way to obtain extensive and highly accurate information on the structure of the turbulent flow, hence, to disclose the very physical roots of the phenomena. At the same time, DNS simulations suffer from the high computational cost which is also the critical issue for the Newtonian fluid case. This helps to explain why very few examples of DNS solutions for non-Newtonian fluids have been reported in the literature, and they all refer to simple, yet at times engineering-relevant geometries, such as straight pipes [10–12].

In order to shed light on the fluid dynamic behaviour of non-Newtonian fluids in complex geometries of engineering interest (e.g. valves, pipe fittings, hydraulic machines), enabling more optimized designs compared to traditional methods, the only possibility is to numerically solve only for the Reynolds-averaged flow field, using Reynolds-Averaged Navier-Stokes (RANS) models. In fact, as it will be further discussed in Section 6.3, experiments have provided global parameters, such as the pressure loss coefficient, which makes laboratory testing a non-valid alternative if deeper insight is needed. At the same time, RANS modelling is much more challenging in non-Newtonian fluids compared to Newtonian ones. As we will see, RANS models for non-Newtonian fluids require evaluating other correlations of fluctuating variables in addition to the Reynolds stresses that also appear for Newtonian fluids. This implies a number of modelling choices, that results in approximations and increased modelling uncertainty. Hence, validating RANS models based on the available DNS data for simple geometries is necessary to give confidence to their results for more complex ones.

Moving forward to some technical details, the basis of RANS models is the Reynolds averaging of each generic fluid dynamic variable ψ, which is referred to as $\overline{\psi}$ and calculated as

$$\overline{\psi} = \lim_{T\to\infty}\frac{1}{T}\int_0^T \psi\, dt \tag{4}$$

and ψ is expressed as the sum of $\overline{\psi}$, which depends only on space, plus a fluctuating component, ψ', which depends on both time and space. Application of the Reynolds-averaging operator (Eq. (4)) to the instantaneous equations (Eqs. (3a) and (3b)) yields

$$\frac{\partial \bar{u}_i}{\partial x_i} = 0 \tag{5a}$$

$$\rho \bar{u}_j \frac{\partial \bar{u}_i}{\partial x_j} = -\frac{\partial \bar{p}}{\partial x_i} + \frac{\partial}{\partial x_j}\left(2\bar{\mu}\bar{s}_{ij} - \rho\overline{u_i' u_j'} + 2\overline{\mu' s_{ij}'}\right) + \rho g_i \tag{5b}$$

where the term $2\overline{\mu' s_{ij}'}$ is specific to the non-Newtonian case, and it is due to the fact that the apparent viscosity fluctuates as a result of fluctuations in the shear rate. The modelling of this term creates an additional challenge compared to the Newtonian case. The Reynolds-stresses term in Eq. (5b), $-\rho\overline{u_i' u_j'}$, is formally the same as in the Newtonian case and, even in non-Newtonian fluids, the Boussinesq's approximation is often employed [13–15] to express this term as a function of an eddy viscosity, μ_t. However, the proper evaluation of the eddy viscosity, as well as of the near-wall turbulence, is not a straightforward task because the commonly-used models available have been developed and validated for Newtonian flows. Broadly speaking, two main approaches have been reported in the literature.

At one extreme, the double correlation $2\overline{\mu' s_{ij}'}$ is neglected in Eq. (5b), and the average viscosity is related to the average shear rate in a form that is analogous to their instantaneous counterparts

$$\bar{\mu} = m(\bar{\dot{\gamma}})^{n-1} \tag{6}$$

where the average shear rate is given as

$$\bar{\dot{\gamma}} = \left(2\bar{s}_{ij}\bar{s}_{ij}\right)^{1/2} \tag{7}$$

This yields the so-called Newtonian Reynolds-Averaged Navier-Stokes (RANS) models, where the viscosity remains undecomposed. Hence, the mass and momentum conservation equations of Newtonian RANS model for power-law fluids read as follows

$$\frac{\partial \bar{u}_i}{\partial x_i} = 0 \tag{8a}$$

$$\rho \bar{u}_j \frac{\partial \bar{u}_i}{\partial x_j} = -\frac{\partial \bar{p}}{\partial x_i} + \frac{\partial}{\partial x_j}\left[2m(\bar{\dot{\gamma}})^{n-1}\bar{s}_{ij} - \rho\overline{u_i' u_j'}\right] + \rho g_i \tag{8b}$$

Typically, Newtonian RANS models use the same turbulence models and near-wall modelling approaches of Newtonian fluids, simply by replacing the constant viscosity with a variable average viscosity obtained through Eq. (6), and possibly making other amendments. Newtonian RANS models are thus simple, generally robust and easy-to-converge, all features that make this approach particularly effective for its application to complex geometries. At the same time, the simplistic treatment of non-Newtonian characteristics might adversely affect its accuracy. And, indeed, there is an open topic of debate in the literature. For instance, regarding the modelling of the near-wall turbulence within the Newtonian RANS framework, Malin [16] showed that the damping function of the Lam-Bremhorst k-ε model [17] can produce reasonable estimates of the friction factor in power-law fluids, but the agreement decreases when n decreases, that is, as the shear thinning behaviour is enhanced. Conversely, other wall functions originally formulated for Newtonian fluids proved unsuitable for non-Newtonian fluids [18–20]. To improve the accuracy of the results for non-Newtonian fluids, a natural approach would be to modify the damping function or wall function. To address the effect of shear thinning and shear thickening on the turbulent viscosity near solid boundaries, Malin [16,21] modified the damping function of the Lam-Bremhorst k-ε model by including the flow index parameter of power-law fluids, obtaining more accurate estimates of friction factors, even for very small n. Within the wall function framework, Sawko [18] adapted the standard wall function to be compatible with the power-law model, achieving good friction factor estimates. Mehta et al. [22] also adopted the methodology outlined by Launder and Spalding [23] to derive a relationship between wall shear stress and velocity in the near-wall cells for a Herschel–Bulkley fluid. The new wall-function showed improvement in the estimation of the wall shear stress and the near-wall velocity field [20]. Also the proper evaluation of the eddy viscosity has not been fully clarified, and it mostly depends on the level of insight that is expected as well as on the parameters that the simulation aims at predicting. For instance, Malin [16] used the Lam-Bremhorst k-ε model, reporting satisfactory friction factor estimates. At the same time, observations in turbulent pipe flows indicate that non-Newtonian properties accentuate turbulence anisotropy [10–12]. This suggests that turbulence models that assume isotropic turbulence, such as the standard k-ε, might result in inaccurate predictions, leading other authors to develop or adopt turbulence models accounting for anisotropic effects.

The two key features of Newtonian RANS models are the neglect of the $2\overline{\mu' s_{ij}'}$ term in the momentum equations, and the evaluation of the average viscosity through Eq. (6). Now, the question arises as: under which conditions are the two simplifications acceptable? With regard to the first feature, Pinho [24] reported that the $2\overline{\mu' s_{ij}'}$ term might be neglected in fluids exhibiting non- or weakly shear-thinning properties in two-dimensional mean flows, such as boundary layers, jets, or pipe flows. Instead, for fully-developed flows where the problem can be treated as one-dimensional, this simplification should be valid, as supported by DNS results of fully-developed turbulent pipe flows of shear-thinning fluids showing that, at $n = 0.8$, $2\overline{\mu' s_{ij}'}$ is a small fraction of the total shear stress [11,12]. For sure, there exists a well-known shortcoming when Newtonian RANS models are applied to shear-thinning, power-law fluids. In fact, Eq. (6) causes $\bar{\mu}$ to approach infinity as $\bar{\dot{\gamma}}$ approaches zero, which is an unphysical result. This produces, in turbulent pipe flows simulations, a significant overestimation of the average apparent viscosity in the core region of the pipe, as it has been reported by Lovato et al. [15] and it will be further highlighted in the present simulation study.

The second approach, at the opposite extreme compared to the Newtonian RANS one, consists of accounting explicitly for the fluctuating viscosity, μ', keeping the $2\overline{\mu' s_{ij}'}$ term in Eq. (5b) and many terms dependent on μ' in the turbulence model. This approach,

which we might call “non-Newtonian RANS” for the sake of simplicity, has a stronger basis, as it is closer to the actual physical equations, and this is an obvious value. At the same time, it appears less practical. Formally speaking, the system of equations to be solved is very complex, which can produce convergence issues especially when complex geometries are simulated. Furthermore, the correlation terms including μ' are not explicitly resolved, but modelled, introducing approximations and a number of closures, coefficients and parameters often not well characterized or difficult-to-decide, which makes the calibration and the testing of the validity of the model outside the calibration conditions more complicated [25].

One of the challenges of non-Newtonian RANS models is how to evaluate the correlation $2\overline{\mu' s'_{ij}}$. Some authors have manipulated Eq. (5b) by expressing the mean and fluctuating viscosity terms as a function of the double correlation $\overline{s'_{ij} s'_{ij}}$, which also appears in the definition of the turbulent dissipation rate, ε, a commonly solved variable in turbulence models. By deriving formulas that contain this double correlation in both viscosity terms, it is possible to define them as a function of ε, which, in turn, is solved through the turbulence model [13,24,14,15]. A significant example of non-Newtonian RANS models is the one of Gavrilov and Rudyak [14]. This model allows overcoming the previously mentioned drawback of Newtonian RANS models that the average apparent viscosity goes to infinity at low shear rates, but it employs an implicit formulation for $\bar{\mu}$, which could make the implementation and the convergence attainment more challenging. In line with their nature and scope, non-Newtonian RANS models often use advanced turbulence models for evaluating the eddy viscosity. For instance, starting from the anisotropic character of power-law fluids, Gavrilov and Rudyak [14] developed a modified formulation of the ζ-f turbulence model of Hanjalić et al. [26], which uses an elliptic relaxation function to capture near-wall turbulence anisotropy. Adhering to similar principles in formulating the non-Newtonian terms, Lovato et al. [15] extended the k–ω equations in the SST model [27] to Herschel-Bulkley fluids.

In summary, there appears to be a trade-off between the simple, easy-to-converge but at times poorly accurate Newtonian RANS models, and the strongly physically-based, but at times complex, difficult-to-calibrate, and challenging-to-converge non-Newtonian RANS models. We recall that the above discussion refers to models based on the RANS approach, but, for the sake of completeness, we recall that CFD simulations of turbulent flow of power-law fluids have been reported also using Large Eddy Simulation (LES), which resolves the scales of the turbulence above a certain threshold and models the remaining ones. Specifically, LES was used in conjunction with wall-stress modelling methods to compute wall-shear stress, which is then used as a boundary condition. Taghvaei and Amani [28] utilized the local velocity correlations for power-law fluids developed by Shenoy and Saini [29] to propose both algebraic and integrated wall-stress modelling methods for turbulent pipe flow. Additionally, they extended the ordinary differential equations for the turbulent boundary layer to account for the rheological behaviour of power-law fluids. This allowed improving predictions of the drag reduction phenomenon observed in shear-thinning fluids. However, although being closer than RANS to the actual behaviour of the physics of turbulence, LES is still computationally quite expensive, which does not make it an engineering-effective tool for practical calculations.

Hence, we revert back to RANS, proposing an engineering-oriented approach for the simulation of shear-thinning power-law fluids, which lies somehow in between Newtonian and non-Newtonian RANS models. Our approach relies on indirect evaluation of the double correlation $2\overline{\mu' s'_{ij}}$ in the momentum equation within the Newtonian RANS framework. As the Newtonian RANS models, it solves Eqs. (5a) and (5b) without the $2\overline{\mu' s'_{ij}}$ term, it evaluates the average apparent viscosity as a function of the average shear rate, and it uses well established low-Reynolds number turbulence models developed for Newtonian fluids without any modification to the damping functions. At the same time, the relation between $\bar{\mu}$ and $\bar{\dot{\gamma}}$ is changed from Eq. (6) to take into account all the approximations made and the fluctuating terms neglected. Specifically, the core idea of our approach, as described in Section 2, is to apply Eq. (6) only at high average shear rates, introducing an empirical correction to limit the rapid increase in apparent viscosity at low shear rates. The transition is controlled by a third parameter in addition to m and n, referred to as the “critical shear rate”, below which the correction is applied. The new approach proved capable of improving the accuracy of the CFD results in the regions of low average shear rates compared to a standard Newtonian RANS model. We anticipate, and we will show, that our approach does not solve the issue of the average apparent viscosity going to infinity as the average shear rate goes to zero. Nonetheless, the rate of increase is slowed down compared to a standard Newtonian RANS model, without the need for implementing iterative correlations that might complicate the convergence for complex flows.

The remainder of this paper is divided in five sections, followed by the conclusions. A detailed presentation of the proposed approach is given in Section 2. The reference solutions and correlations used for the development and testing of the new approach are presented in Section 3. Details of the CFD set-up are given in Section 4. Section 5 is dedicated to the calibration and validation of the proposed modelling framework, including the comparison against a standard Newtonian RANS model. Finally, Section 6 discusses relevant modelling aspects and presents a comparison against the implicit average apparent viscosity function of Gavrilov and Rudyak [14].

2. The proposed approach

The proposed modelling approach fits into the simple Newtonian RANS framework, in which the double correlation $2\overline{\mu' s'_{ij}}$ is neglected, the average apparent viscosity, $\bar{\mu}$, is a function of the average shear rate $\bar{\dot{\gamma}}$, and the classical Newtonian turbulence models and wall treatment methods are employed. As an indirect way to account for the simplifications and approximations made, our idea is to replace the typical evaluation of $\bar{\mu}$ with a more general relation. Hence, the following formulation of the averaged mass and momentum conservation equations is solved,

$$\frac{\partial \bar{u}_i}{\partial x_i} = 0 \tag{9a}$$

$$\rho\bar{u}_j\frac{\partial\bar{u}_i}{\partial x_j}=-\frac{\partial\bar{p}}{\partial x_i}+\frac{\partial}{\partial x_j}\left[2\bar{\mu}\left(\bar{\dot{\gamma}}\right)\bar{s}_{ij}-\rho\overline{u_i'u_j'}\right]+\rho g_i \tag{9b}$$

The relation between the average apparent viscosity and the average shear rate is Eq. (6) at high shear rates, whereas a logarithmic function is employed at low shear rates. The transition between these two functions is controlled by the parameter $\bar{\dot{\gamma}}_c$, referred to as the "critical shear rate". The resulting average apparent viscosity function is illustrated graphically in Fig. 1 and described analytically by the following equation

$$\bar{\mu}(\bar{\dot{\gamma}})=\begin{cases}a\ln\bar{\dot{\gamma}}+b & \text{for } \bar{\dot{\gamma}}<\bar{\dot{\gamma}}_c\\ m\bar{\dot{\gamma}}^{n-1} & \text{for } \bar{\dot{\gamma}}\geq\bar{\dot{\gamma}}_c\end{cases} \tag{10}$$

where

$$a=m(n-1)\left(\bar{\dot{\gamma}}_c\right)^{n-1} \tag{11}$$

$$b=m\left[1-(n-1)\ln\bar{\dot{\gamma}}_c\right]\left(\bar{\dot{\gamma}}_c\right)^{n-1} \tag{12}$$

Note that the expressions for the two coefficients a and b were obtained by ensuring continuity of the Reynolds-averaged apparent viscosity and its slope at the critical shear rate, guaranteeing a smooth transition between the power-law model and the logarithmic branch.

The use of Eq. (10) instead of Eq. (6) over the entire range of average shear rates, as done in Newtonian RANS models, provides significant advancement. As explained in the Introduction, an obvious shortcoming of the classical Newtonian RANS formulation applied to fully developed pipe flow of shear-thinning power law fluids is that the apparent viscosity tends to infinity very quickly in the centreline of the pipe, which is a consequence of the fact that $\bar{\mu}$ tends to infinity very quickly for $\bar{\dot{\gamma}}\to 0$. Our formulation does not prevent $\bar{\mu}$ tending to infinity at the centreline of pipe flow, but makes $\bar{\mu}$ approach infinity at a reduced rate. This not only improves the accuracy of the predictions for fully developed pipe flow, but it also helps the convergence attainment for this and other types of flows. It must be remarked that, in our simulations, where the single slab solver of [30] was used to iteratively obtain the solution for fully-developed pipe flow, the convergence behaviour was consistently good even when using the classical Newtonian RANS formulation. However, convergence problems have been well documented in fluids with a yield stress [31], and they were also reported in strongly shear-thinning fluids [32].

Three additional remarks can be made regarding the proposed average apparent viscosity function. Firstly, existing non-Newtonian RANS models, such as that of Gavrilov and Rudyak [14], produce a finite $\bar{\mu}$ at the pipe axis. In Section 6.2, we will show that this good feature is preserved also when employing, within the standard Newtonian RANS framework, the mean apparent viscosity function of Gavrilov and Rudyak, which is just a single element of the more complex non-Newtonian RANS framework described in [14]. However, the implicit formulation of the apparent viscosity function makes the numerical solution procedure more complex and at times challenging, and increases the simulation time. Clearly, this is not an issue for the present fully developed pipe flow simulations, which are very fast, but it might become a critical problem for more complex geometries. A second consideration concerns the choice of the logarithmic branch to describe the dependence of $\bar{\mu}$ on $\bar{\dot{\gamma}}$ at low shear rate. The idea of using a logarithmic branch does not have a theoretical basis, but it comes from the observation that DNS results of turbulent-pipe flows of power-law fluids have shown that for $n<1.0$, the average viscosity profile follows a logarithmic-like trend in part of the buffer layer and log-layer [11], and that the extent of this region increases with Reynolds number [12]. The log-like behaviour has also been observed in DNS results of fully-developed turbulent channel flows of shear-thinning fluids described by the power-law model [33], and in shear-thinning fluids that also consider a limit constant viscosity at a very low shear rate [34]. A final comment concerns the parameters of the apparent viscosity function. In our formulation, three parameters must be set, namely m, n, and $\bar{\dot{\gamma}}_c$. However, they are of a different nature and scope. In fact, m and n relate to the rheology of the fluid, and they can be obtained through a rheometer. Conversely, $\bar{\dot{\gamma}}_c$ is a parameter that governs the transition between the power-law model in the high shear rate region and the empirical logarithmic function in the low shear-rate region. The determination of the appropriate value of $\bar{\dot{\gamma}}_c$ for the pipe flow cases of interest will be illustrated later in Section 5.2.

In addition to defining the average apparent viscosity, $\bar{\mu}$, Eq. (9b) requires appropriate closures for the correlation $-\rho\overline{u_i'u_j'}$, and specific near-wall treatment methods. As already mentioned, with the goal of keeping the model formulation as simple as possible, we decided to make use of three well established turbulence models originally developed for Newtonian fluids and based on the "low-Reynolds-number" approach, in which the flow in the near-wall region is resolved up to within the viscous sublayer. These models are the Lam-Bremhorst k-ε model [17], two-layer k-ε model [35], and k-ω SST model [27], and, for brevity, we refer to these models as LB, 2L, and SST, respectively. All these models rely on the eddy-viscosity assumption of Boussinesq, that is

$$-\rho\overline{u_i'u_j'}=2\mu_t\bar{s}_{ij}-\frac{2}{3}\rho\delta_{ij}k \tag{13}$$

where μ_t is the eddy (turbulent) viscosity and δ_{ij} is the Kronecker symbol.

Substituting Eq. (13) into Eq. (5b) yields

$$\rho\bar{u}_j\frac{\partial\bar{u}_i}{\partial x_j}=-\frac{\partial}{\partial x_i}\left(\bar{p}+\frac{2}{3}k\right)+\frac{\partial}{\partial x_j}\left[\left(\bar{\mu}+\mu_t\right)\left(\frac{\partial\bar{u}_i}{\partial x_j}+\frac{\partial\bar{u}_j}{\partial x_i}\right)\right]+\rho g_i \tag{14}$$

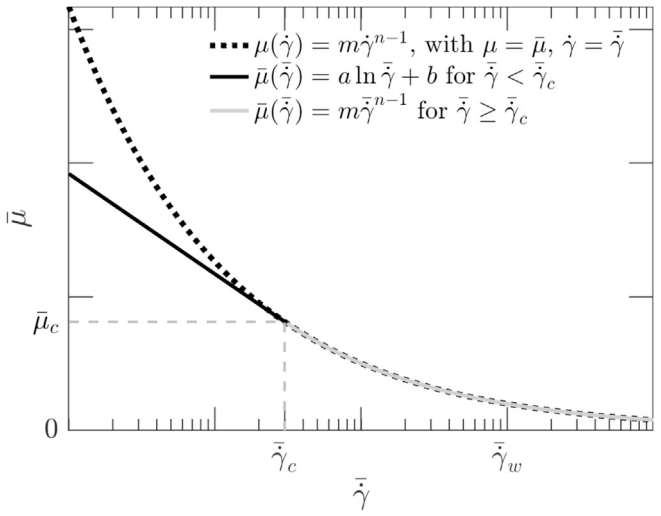

Fig. 1. The shear-thinning power-law model in the traditional RANS-based approach and the proposed average apparent viscosity function. Note that the plot is a semi-log one.

and the formula for μ_t, as well as the parameters on which this variable depends, are specific to the turbulence model used. The LB and 2L models incorporate transport equations for the turbulent kinetic energy, k, and the dissipation rate, ε. The transport equation for k can be obtained from manipulation of the instantaneous and Reynolds averaged equations, and reads as follows,

$$\rho \bar{u}_j \frac{\partial k}{\partial x_j} = \overbrace{\mu_t \bar{s}_{ij}^2}^{\mathcal{P}} + \overbrace{\frac{\partial}{\partial x_j}\left[\left(\bar{\mu} + \frac{\mu_t}{\sigma_{t,k}}\right)\frac{\partial k}{\partial x_j}\right]}^{\mathcal{T}+\Pi+D} - \rho\varepsilon \tag{15}$$

where the transport of variable k is determined by a balance between the production term, $\mathcal{P}$, the dissipation term, $-\rho\varepsilon$, and three other terms (namely, the turbulent velocity transport $\mathcal{T}$, the pressure-related transport Π, and the mean viscous transport D), which are modelled by a single diffusive term. Inside this term, $\sigma_{t,k} = 1$ corresponds to the turbulent Prandtl number for k. Note that, consistent with our modelling approach, the average apparent viscosity $\bar{\mu}$ in Eq. (15) is evaluated through Eq. (10). The transport equation for the dissipation rate, ε, is completely empirical, and its structure is formally analogous to that of k,

$$\rho \bar{u}_j \frac{\partial \varepsilon}{\partial x_j} = \frac{\partial}{\partial x_j}\left[\left(\bar{\mu} + \frac{\mu_t}{\sigma_{t,\varepsilon}}\right)\frac{\partial \varepsilon}{\partial x_j}\right] + C_{1\varepsilon}\overbrace{\mu_t \bar{s}_{ij}^2}^{\mathcal{P}}\frac{\varepsilon}{k} - C_{2\varepsilon}\rho\frac{\varepsilon^2}{k} \tag{16}$$

where $\sigma_{t,\varepsilon} = 1.3$ is the turbulent Prandtl number for ε, and $C_{1\varepsilon} = 1.44$ and $C_{1\varepsilon} = 1.92$ are model constants. Both the LB and 2L models solve for Eqs. (15) and (16) far from the wall. However, near the wall, the formulation varies depending on the turbulence model used. In the LB model, the damping function f_μ is introduced to adjust the empirical constants $C_\mu = 0.09$ in the eddy-viscosity equation within the near-wall region [17]:

$$\mu_t = f_\mu C_\mu k^2/(\rho\varepsilon) \tag{17}$$

$$f_\mu = [1 - \exp(-0.0165\mathrm{Re}_n)]^2(1 + 20.5/\mathrm{Re}_\mathrm{T}) \tag{18}$$

where Re_n and Re_T are Reynolds numbers defined as:

$$\mathrm{Re}_n = \rho k^{1/2} y/\bar{\mu} \tag{19}$$

$$\mathrm{Re}_\mathrm{T} = \rho k^2/(\varepsilon\bar{\mu}) \tag{20}$$

with y as the distance to the wall. Additionally, the damping functions f_1 and f_2 multiply the constants $C_{1\varepsilon}$ and $C_{2\varepsilon}$ in the transport equations of ε [17], respectively:

$$f_1 = 1 + (0.05/f_\mu)^3 \tag{21}$$

$$f_2 = 1 - \exp(-\mathrm{Re}_\mathrm{T}^2) \tag{22}$$

On the other hand, the 2L model employs the one-equation model of Norris and Reynolds [36] to solve the near-wall region [35]. In this region, the dissipation rate is determined by:

$$\varepsilon = k^{3/2}/\ell_\varepsilon \tag{23}$$

$$\ell_\varepsilon = \kappa y/[C_\mu^{3/4}(1 + 5.3/\mathrm{Re}_n)] \tag{24}$$

where ℓ_ε is a length scale and $\kappa = 0.41$ is the von Kármán constant. The eddy-viscosity is calculated as:

$$\mu_t = C_\mu k^{1/2}\ell_\mu/\rho \tag{25}$$

$$\ell_\mu = \kappa y C_\mu^{-3/4}[1 - \exp(-0.0198\mathrm{Re}_n)] \tag{26}$$

where ℓ_μ is another length scale. The one-equation model is matched with the standard k-ε turbulence model at locations where $\mathrm{Re}_n = 350$.

The k-ω SST model solves for the turbulent kinetic energy and the turbulent frequency, ω. The transport equation for k is slightly different to that of the LB and 2L models, and it reads as follows,

$$\rho\bar{u}_j\frac{\partial k}{\partial x_j} = \overbrace{\min\left(\mu_t\bar{s}_{ij}^2, 10\beta^*\rho k\omega\right)}^{\mathcal{P}} + \overbrace{\frac{\partial}{\partial x_j}\left[\left(\bar{\mu} + \sigma_k\mu_t\right)\frac{\partial k}{\partial x_j}\right]}^{\mathcal{T}+\Pi+D} - \rho\overbrace{\beta^* k\omega}^{\varepsilon} \tag{27}$$

whereas the transport equation for ω is obtained empirically, and it takes the following form

$$\begin{aligned}\rho\bar{u}_j\frac{\partial \omega}{\partial x_j} = {} & \rho\omega\gamma\frac{\min\left(\mu_t\bar{s}_{ij}^2, 10\beta^*\rho k\omega\right)}{k} + \frac{\partial}{\partial x_j}\left[\left(\bar{\mu} + \sigma_\omega\mu_t\right)\frac{\partial \omega}{\partial x_j}\right] \\ & - \rho\beta\omega^2 + 2\left(1 - F_1\right)\rho\sigma_{\omega 2}\frac{1}{\omega}\frac{\partial k}{\partial x_i}\frac{\partial \omega}{\partial x_i}\end{aligned} \tag{28}$$

The SST model preserves the k-ω model formulation in the region near the wall, while utilizing the k-ε model in the outer portion of the boundary layer. To accomplish this, the k-ε model is converted into a k-ω formulation using a blending function F_1. The constants σ_k, σ_ω, β, and γ change with the formulation, whereas $\beta^* = 0.09$ is always the same. In the k-ω formulation, the constants used are: $\sigma_k = 0.5$, $\sigma_\omega = 0.5$, and $\beta = 0.075$; on the other hand, for the k-ε formulation, the constants are $\sigma_k = 1.0$, $\sigma_\omega = 0.856$, and $\beta = 0.0828$. Note that the difference between the formulations of the k equations in the SST, LB and 2L models resides only in the evaluation of the production term, $\mathcal{P}$, as well as in the definition of the constant in the diffusive term. Conversely, the dissipation terms are the same, and this gives the relation between k, ε, and ω, as follows,

$$\varepsilon = \beta^* k\omega \tag{29}$$

3. Test cases

The proposed approach was initially developed and tested for pipe transport of shear-thinning power-law fluids, so that DNS data available in the literature could be exploited to make a throughout validation of its capabilities. However, we recall that our method is mostly intended as a practical tool for application to more complex flows, which is, in principle, feasible but could require future refinement (see Section 6.3). The pipe flow test cases considered in this study were identified through combinations of two dimensionless parameters, namely, the flow index parameter, n, which appears in the rheological model (Eq. (2)), and the friction Reynolds number, Re_τ, defined as

$$\mathrm{Re}_\tau = u_\tau R/\nu_w \tag{30}$$

in which R is the radius of the pipe, equal to half its diameter D, u_τ is the shear velocity, and ν_w is the kinematic apparent viscosity at the wall. Both u_τ and ν_w are functions of the wall shear stress, since

$$u_\tau = \sqrt{\tau_w/\rho} \tag{31}$$

and

$$\nu_w = \rho^{-1}m^{1/n}\tau_w^{1-1/n} \tag{32}$$

which was obtained by applying Eqs. (1) and (2) at the pipe wall. In this study, four values of $n = [0.4\ 0.6\ 0.8\ 1.0]$ and ten values of $\mathrm{Re}_\tau = [323\ 500\ 750\ 1000\ 1250\ 1500\ 1750\ 2000\ 2250\ 2500]$ were considered, resulting in forty simulated flow conditions. Out of the four values of n, three correspond to shear thinning fluids (0.4, 0.6, 0.8), and one to a Newtonian fluid (1.0). Considering $n = 1.0$ provides a basis of comparison with respect to the Newtonian case. Each case was run with the three turbulence models (LB, 2L, and SST) described in Section 2.

For calibration and validation, we employed the DNS data from Singh et al. [11,12] and two empirical correlations for the frictional losses [37,38]. The DNS data refer to a subset of the eight combinations of n and Re_τ, as detailed in Table 1. Out of these eight cases, five of them are non-Newtonian. Regarding $n = 0.4$, the authors only reported the friction factor because the flow exhibited a transitional nature [11]. As far as the empirical formulas are concerned, these relate the Fanning friction factor, f,

Table 1
Flow conditions of the DNS cases from Singh et al. [11,12].

n	0.4	0.6	0.6	0.6	0.8	1.0	1.0	1.0
Re_τ	323	323	500	750	323	323	500	750

$$f = 2\tau_w / \left(\rho U_b^2\right) \tag{33}$$

to the flow index n and the Reynolds number of Metzner and Reed [39], $\mathrm{Re}_{\mathrm{MR}}$,

$$\mathrm{Re}_{\mathrm{MR}} = \frac{8\rho U_b^{2-n} D^n}{m\left(6+\frac{2}{n}\right)^n} \tag{34}$$

where U_b is the bulk velocity of the flow in the pipe. However, each test case was defined by the friction Reynolds number Re_τ instead of $\mathrm{Re}_{\mathrm{MR}}$. To relate these two Reynolds numbers, we use the definition of the Fanning friction factor (Eq. (33)). Consequently, $\mathrm{Re}_{\mathrm{MR}}$ is connected to Re_τ as follows:

$$\mathrm{Re}_{\mathrm{MR}} = \frac{\mathrm{Re}_\tau^n 2^{4-\frac{n}{2}}}{\left(3+\frac{1}{n}\right)^n f^{1-\frac{n}{2}}} \tag{35}$$

This definition of $\mathrm{Re}_{\mathrm{MR}}$ (Eq. (35)) is then substituted into two different formulas for turbulent flows of power law fluids in smooth pipes. The former is the well-known empirical correlation of Dodge and Metzner [37]

$$\frac{1}{\sqrt{f}} = \frac{4.0}{n^{0.75}} \log_{10}\left(\mathrm{Re}_{\mathrm{MR}} f^{(2-n)/2}\right) - \frac{0.4}{n^{1.2}} \tag{36}$$

which, when $n = 1$, reduces to the Karman-Nikuradse correlation for Newtonian fluids. In [37], the validated range of parameters depends on the value of n. For n equals to 0.8, 0.6 and 0.4, the maximum validated $\mathrm{Re}_{\mathrm{MR}}$ was approximately 40,000, 30,000 and 10,000, respectively. When substituting Eq. (35) into Eq. (36), an alternative version of the correlation is obtained, which is a function of Re_τ and explicit in f

$$\frac{1}{\sqrt{f}} = \frac{4.0}{n^{0.75}} \log_{10}\left[\frac{\mathrm{Re}_\tau^n 2^{4-\frac{n}{2}}}{\left(3+\frac{1}{n}\right)^n}\right] - \frac{0.4}{n^{1.2}} \tag{37}$$

The second model is the expression proposed by Anbarlooei et al. [38], which is based on the Blasius correlation:

$$f = \left(0.102 - 0.033n + \frac{0.01}{n}\right) \frac{1}{\mathrm{Re}_{\mathrm{MR}}^{1/[2(n+1)]}} \tag{38}$$

The authors compared the model against the experimental data of shear-thinning fluids. For $n = 0.7$, the maximum $\mathrm{Re}_{\mathrm{MR}}$ was approximately 40,000, and, for $n = 0.45$, it was approximately 20,000. By substituting Eq. (35) into Eq. (38), the correlation is expressed as a function of Re_τ, as follows:

$$f = \left(0.102 - 0.033n + \frac{0.01}{n}\right)^{\frac{4(n+1)}{5n+2}} \left(\frac{\left[3+\frac{1}{n}\right]^n}{\mathrm{Re}_\tau^n 2^{4-\frac{n}{2}}}\right)^{\frac{2}{5n+2}} \tag{39}$$

4. CFD model

The simulations were carried out in the dimensional framework; hence, the first task was to define the geometry and boundary conditions of the CFD setup corresponding to a given combination of n and Re_τ. A fixed pressure gradient was imposed, which was obtained from $-\partial p/\partial z = 2\tau_w/R$. This requires knowing the pipe radius, R, and the wall shear stress, τ_w, the latter being calculated from the friction velocity, u_τ, through Eq. (31). According to the conditions imposed by Singh et al. [11,12], $\nu_w = 1/\mathrm{Re}_\tau$ [m^2/s], which implies that $u_\tau R = 1$ [m^2/s], which was obtained with $R = 0.5$ [m] and $u_\tau = 2$ [m/s]. As far as the rheological parameters of the fluid are concerned, n [-] was one of two input parameters, whereas m [Pa s^n] was obtained from Eq. (32). The bulk velocity U_b was calculated as an output from the simulation. This, in turn, allowed evaluating a posteriori the Fanning friction factor (Eq. (33)) and the Reynolds number of Metzner and Reed (Eq. (34)).

The code PHOENICS 2022 was used for the numerical solution of the flow equations through a finite-volume procedure. The proposed average apparent viscosity model (Eq. (10)) was implemented in the input file Q1 through the In-Form utility, with minor modifications in the PHOENICS Input Language (PIL) code. The flow was treated as steady-state, one-dimensional, axisymmetric, and fully-developed. Thus, the computational domain in the axial direction was represented by a single slab of cells, and, due to

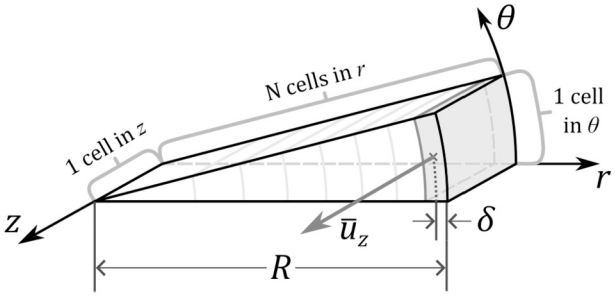

Fig. 2. Scheme of a slice of pipe representing the computational domain.

axi-symmetry, the only space coordinate is the radial one, r, as illustrated in Fig. 2. A structured staggered-grid arrangement is employed, with scalar variables computed at the cell centroids and velocities at the cell faces. The longitudinal pressure gradient, $(-\partial p/\partial z)$, was imposed, and the primary output variables are the Reynolds averaged axial velocity component, $\bar{u}_z$, and the turbulent parameters, namely, k and, depending on the used turbulence model, ε or ω. All variables use the hybrid-differencing scheme, which employs the first-order upwind-differencing scheme in high-convection regions, and the second-order central-differencing scheme in low-convection regions. At the axis of the pipe, a zero-flux condition is employed for all variables. At the pipe wall, a no-slip condition was enforced for the velocity, whereas the wall-boundary conditions for the turbulent variables are $k = 0$ at the wall, zero-normal gradient for ε over the wall face area (LB and 2L models), and $\omega = 2\bar{\mu}/\left(\rho C_{2\omega}\delta^2\right)$ in the centre of the near-wall cell (SST model), where $C_{2\omega} = 3/40$ is a constant of the k-ω SST model and δ represents the distance between the centre of the near-wall cell and the wall (Fig. 2). In the one-dimensional model, the design of the computational mesh consists in defining the sub-divisions along the radial direction, r. A grid-independence study involved four meshes and it was carried out for all simulations. Each designed grid has a refinement ratio of two with respect the previous one. The grid spacing follows a geometric progression rule, increasing from the wall to the pipe centre. The finest grid consists of 400 cells and a progression ratio of 1.02. Additionally, as a recommendation for RANS simulations using k-ω SST model, the size of the nearest cell to the wall was adjusted to fulfil $y^+ \lesssim 0.1$ [40] for all meshes and all turbulence models.

The single-slab solver is used to iteratively obtain the numerical solution according to the procedure described in [30]. In all calculations, double precision was used and the selected global convergence criterion for the normalized, whole-field residuals was set equal to 10^{-6}; the number of iterations to reach convergence was of the order of 10^3 when using the LB and 2L models, whereas it was of the order of 10^2 with the SST model.

5. Numerical results

The numerical results obtained from the application of the proposed methodology are now presented. As a basis for comparison, we considered both the DNS data from Singh et al. [11,12] the two empirical correlations from the friction factor (Eqs. (36) and (38)) and the results obtained with the classical, Newtonian RANS framework in which the mean apparent viscosity is evaluated through Eq. (6). Our approach requires determining the critical shear rate in Eq. (10), that is, $\bar{\dot{\gamma}}_c$, below which the relation between the apparent viscosity and the shear rate switches from the power-law rheology model to the logarithmic branch. The procedure for the calibration of $\bar{\dot{\gamma}}_c$ is described in Section 5.2. Afterwards, Sections 5.3 to 5.7 illustrate the validation results for different flow parameters. However, we start by reporting some preliminary considerations on the non-dimensional variables and terminology used to represent the flow.

5.1. Non-dimensional variables and structure of the flow

For the sake of generality, the results are presented in dimensionless form, introducing appropriate wall scales. As mentioned before, the nominal wall viscosity ν_w is the selected viscosity scale. As such, the normalized averaged apparent viscosity is $\bar{\mu}^+ = \bar{\mu}/(\rho\nu_w)$. The friction velocity u_τ is used as the velocity scale and ν_w/u_τ is employed as the length scale. The distance from the wall is $y = R - r$; hence, the non-dimensional mean axial velocity and wall distance are expressed as $\bar{u}_z^+ = \bar{u}_z/u_\tau$ and $y^+ = y/(\nu_w/u_\tau)$, respectively. The combination of both variables results in the normalized mean velocity gradient $\partial\bar{u}_z^+/\partial y^+ = (\partial\bar{u}_z/\partial y)(\nu_w/u_\tau^2)$. For the shear-stress-budget study, stresses terms are normalized by $\tau_w = \rho u_\tau^2$. The turbulent kinetic energy k is normalized by u_τ^2. The production, transport and dissipation of k are normalized by $\rho u_\tau^4/\nu_w$. Finally, the Fanning friction factor, f (Eq. (33)), is used to quantify the frictional losses.

Another consideration relates to the fact that the structure of the boundary layer in power law fluids is not as obvious as in Newtonian fluids [11]. Semi-theoretical expressions for power-law fluids have subdivided the flow in a similar way to the Newtonian case [37,41,42,29], but the precise location of the boundaries for each region is unclear. In order to simplify the analysis, the same regions and limits defined for turbulent flows of Newtonian fluids are here considered. Hence, we will refer to viscous sublayer ($y^+ < 5$), buffer layer ($5 < y^+ < 30$), log-law region ($30 < y^+ < 200$), and core region ($y^+ > 200$).

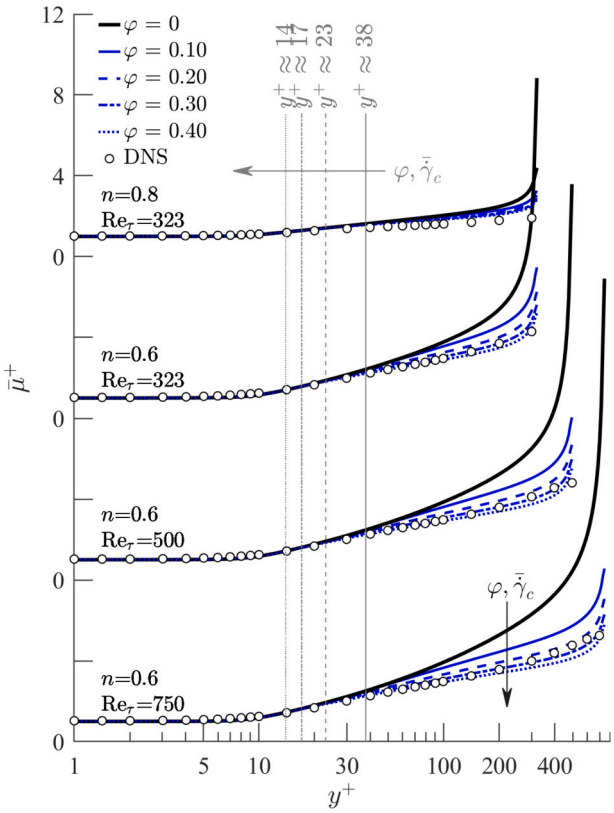

Fig. 3. The effect of φ on the calibration of the average apparent viscosity function (Eq. 10) for the LB model. The viscosity profiles are compared with DNS data from Singh et al. [11,12]. Vertical grey lines indicate the y^+ locations of the critical shear rate for different values of φ.

5.2. Critical shear rate and Reynolds-averaged apparent viscosity

The criterion to select the appropriate value of $\bar{\dot{\gamma}}_c$ was the agreement between the Reynolds-averaged apparent viscosity profile $\bar{\mu}$ obtained from the simulations and the DNS data reported in the literature. Specifically, four shear-thinning cases among those described in Table 1, were considered, characterized by $n = 0.6$ or 0.8. Additionally, the value of $\bar{\dot{\gamma}}_c$ was verified by analysing its location within the turbulent boundary layer, as well as the effect of its potential variability.

Wilson and Thomas [43] explain that the thickness of the viscous sublayer increases when the size of the dissipative micro-eddies is also increased. They further note that, for the same wall shear stress, a thicker viscous sublayer results in a higher bulk velocity, which is considered a drag reduction mechanism. The thickness of the viscosity-dependent region increases with stronger shear-thinning effects [11], and slightly increases with Re_τ [12]. Consequently, the onset of the log-like region may depend on both n and Re_τ. The average apparent viscosity profiles reported in the reference DNS data [11,12] indicate that the log-like region is present for $y^+ \gtrsim 20$. However, this description is general and their results do not examine how the onset of the log-like region varies as a function of n or Re_τ, posing a challenge for the calibration of our methodology. Therefore, to determine the appropriate value of $\bar{\dot{\gamma}}_c$, different values were tested, expressed as fractions of the shear rate at the wall, $\bar{\dot{\gamma}}_w$, that is,

$$\bar{\dot{\gamma}}_c = \varphi \bar{\dot{\gamma}}_w \tag{40}$$

with $0 \leq \varphi < 1$. It is important to note that, in fully-developed turbulent pipe flows, the only velocity gradient that displays non-zero values is $\partial \bar{u}_z/\partial r$ (or $\partial \bar{u}_z/\partial y$), which decreases in magnitude as the distance from the wall increases. Consequently, the Reynolds-averaged shear rate (Eq. (6)) is expressed as $\bar{\dot{\gamma}} = \partial \bar{u}_z/\partial y$, or in dimensionless form, $\bar{\dot{\gamma}}^+ = \partial \bar{u}_z^+/\partial y^+$. For Newtonian fluids, the Reynolds-averaged shear rate at the wall is $\bar{\dot{\gamma}}_w^+ = 1$. However, in shear-thinning fluids, $\bar{\dot{\gamma}}_w^+$ can be slightly greater than one due to non-zero viscosity fluctuations at the wall [11]. In our approach, since the Newtonian-based RANS formulation is employed, all cases —including the shear-thinning fluids— display $\bar{\dot{\gamma}}_w^+ = 1$. Thus, the parameter φ is equivalent to the dimensionless Reynolds-averaged shear rate value at which the transition between the Reynolds-averaged analogue of the power law model and logarithmic function occurs. From this, an approximate value of y^+ can be inferred.

Fig. 3 shows the effect of φ on the average apparent viscosity profiles obtained with the LB model, presented in dimensionless form as $\bar{\mu}^+$ versus y^+, for four combinations of n and Re_τ. For each case, the average apparent viscosity profile was plotted for $\varphi = 0$ (solid black line), which corresponds to the classical Newtonian RANS model, as well as $\varphi = 0.15$ (solid blue line), $\varphi = 0.20$ (dashed blue line), $\varphi = 0.30$ (dash-dotted blue line), and $\varphi = 0.40$ (dotted blue line). The vertical grey lines approximately indicate

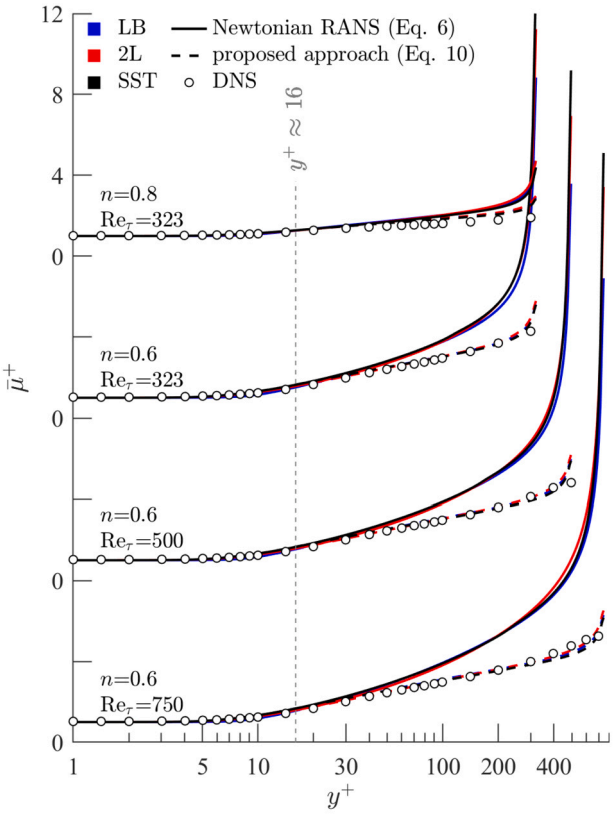

Fig. 4. Normalized profiles of the Reynolds-averaged apparent viscosity for different combinations of n and Re_τ. The plots compare our simulation results with and without the critical shear rate, as obtained from three turbulence models, and the DNS data from Singh et al. [11,12].

the onset of the logarithmic function in all cases, which decreases from $y^+ \approx 38$ to $y^+ \approx 14$ when φ increases from 0.10 to 0.40. This range of values appears physically sound, since they are around $y^+ = 20$ and most of them are in the buffer layer. Moreover, increasing φ reduces the average apparent viscosity in the log-law and core regions. Note that the case with $n = 0.8$ (upper block) is almost insensitive to variations in φ, and further increasing in φ to reduce the average apparent viscosity in the log-like region will make the onset of the logarithmic function fall within the viscous sub-layer. In contrast, the cases with $n = 0.6$ (last three blocks) exhibit greater sensitivity to variations in φ. For all the evaluated Re_τ values at $n = 0.6$, the best agreement with the DNS results was obtained with $\varphi = 0.30$, although the difference in the core region appears to increase at higher Re_τ. The effect of φ on all cases for the 2L and SST models was found to be the same (showed in the next Figure). The limited number of cases for which DNS data are available precluded the possibility of proposing a formula to estimate the appropriate φ (or $\bar{\dot{\gamma}}_c$) depending on n and Re_τ. Based on the data at our disposal, the recommended value for φ was decided as 0.30, noting that, for cases where $n < 0.6$, the average apparent viscosity profile is expected to be underestimated.

Fig. 4 presents a comparison of the average apparent viscosity profiles obtained using the three turbulence models for four combinations of n and Re_τ. Each case includes the results of our approach with the calibrated value of $\varphi = 0.30$ (dashed lines), the Newtonian RANS solution with $\varphi = 0$ (solid lines), and the DNS data from Singh et al. [11,12] (unfilled circles). The colours of the lines denote the turbulence model used in our RANS simulations, namely, LB (blue), 2L (red), and SST (black). Overall, for a fixed value of φ, the viscosity profiles are similar regardless of the turbulence model used. Comparison of the continuous lines with the unfilled circles indicates that applying the power law model to the Reynolds-averaged apparent viscosity causes its value to grow indefinitely from the wall to the core, overestimating the DNS data for y^+ higher than say 20, i.e. from the buffer layer towards the centre of the pipe. This overestimation becomes significant in the core region, increasing with lower n (first and second blocks from the top) or higher Re_τ (last three blocks). Conversely, the modified average apparent viscosity model with $\varphi = 0.30$ activates the logarithmic branch for $y^+ \gtrsim 16$ (dashed grey line), resulting in good agreement of the averaged apparent viscosity profile with the DNS data. In the core region, the agreement worsens slightly because, as the shear rate approaches zero, the viscosity approaches infinity, but at a much slower rate compared to the classical Newtonian RANS model, which translates into smaller values of apparent viscosity in the computational cell adjacent to the pipe axis. As mentioned before, the viscosity profile for $n = 0.8$ overestimates the DNS data (first block from the top); however, such overestimation is relatively mild in absolute terms and, anyway, our approach improves the degree of agreement compared to the classical Newtonian RANS model.

Table 2
Percentage error of the friction factor obtained from our simulations relative to DNS data [11,12].

n	Re_τ	LB			2L			SST		
		Newt. RANS $\mu = \rho/Re_\tau$	Newt. RANS Eq. (6)	Prop. app. Eq. (10)	Newt. RANS $\mu = \rho/Re_\tau$	Newt. RANS Eq. (6)	Prop. app. Eq. (10)	Newt. RANS $\mu = \rho/Re_\tau$	Newt. RANS Eq. (6)	Prop. app. Eq. (10)
1.0	323	0.7	0.7	–	9.6	9.6	–	-1.3	-1.3	–
	500	2.5	2.5	–	8.4	8.4	–	-2.9	-2.9	–
	750	3.7	3.7	–	7.1	7.1	–	-4.0	-4.0	–
0.8	323	7.8	-4.2	-3.9	17.4	4.6	5.5	5.7	4.9	5.0
0.6	323	17.7	-12.4	-10.3	28.1	0.8	3.9	15.4	13.1	14.0
	500	20.5	-10.2	-7.7	27.5	1.9	2.2	14.2	11.5	12.5
	750	20.8	-9.7	-6.8	24.8	-4.7	0.1	11.8	8.9	9.9
0.4	323	33.3	-26.8	-19.2	45.1	4.0	7.8	30.7	25.6	29.2

5.3. Friction factor

The ability of our approach in estimating the frictional losses was investigated by reference to the Fanning friction factor, developing the analysis at three levels.

Firstly, the individual cases from the DNS literature (Table 1) are used as reference to assess the performance of our numerical results. The percentage relative error of the friction factor obtained from our simulations relative to DNS data [11,12] is depicted in Table 2 for the combinations of n and Re_τ in Table 1. The error is calculated for each turbulence model using three approaches: the RANS modelling of a Newtonian fluid with constant viscosity ($\mu = \rho/Re_\tau$), to evaluate the impact of neglecting shear-thinning effects; the classical Newtonian RANS formulation ($\varphi = 0$), as the simplest way to account for shear-thinning effects; and our proposed approach ($\varphi = 0.30$), to assess the impact of improving the viscosity estimation far from the wall. For $n < 1.0$, using a constant viscosity of $\mu = \rho/Re_\tau$ leads to an overestimation of the friction factor, which becomes more pronounced as n decreases. The magnitude of this overestimation is consistently greater than the error obtained with the Newtonian RANS model. Since the wall shear stress remains the same across all simulations, the overestimation caused by neglecting shear-thinning effects is attributed to a lower bulk velocity U_b. The benefit of switching from the Newtonian RANS model ($\varphi = 0$) to our approach ($\varphi = 0.30$) strongly depends on the turbulence model used. Using the LB model, our approach improved the estimation of the friction factor, whereas no improvement, and even a slight overall deterioration, can be detected with the 2L and SST models. Significant worsening in the prediction accuracy was observed with the 2L and SST models for the case with $n = 0.4$, which, as already mentioned in the literature, exhibited transitional nature. The 2L model demonstrated the smallest relative errors across the majority of the shear-thinning cases, and these errors were even smaller than those for $n = 1.0$.

Secondly, a global indicator is employed to evaluate the deviation between our simulations and the friction factor estimates from the literature correlations presented in Section 3. Specifically, we referred to the Mean Absolute Percentage Error (MAPE), which is defined as

$$\mathrm{MAPE} = \frac{1}{N}\sum_{i=1}^{N}\frac{|f_{\mathrm{CFD},i} - f_{\mathrm{ref},i}|}{f_{\mathrm{ref},i}} \cdot 100 \tag{41}$$

where i represents the individual data point, N is the total number of data points, f_{CFD} is the friction factor obtained from our simulation, and f_{ref} is the friction factor from any of the two literature correlations. The results are summarized in Table 3. The MAPE values were calculated for four values of n (1.0, 0.8, 0.6 and 0.4), and ten values of Re_τ (323, 500, 750, 1000, ..., 2500). Once again, the error is calculated for each turbulence model referring to a Newtonian fluid model with constant artificial viscosity $\mu = \rho/Re_\tau$, the Newtonian RANS model ($\varphi = 0$), and our approach ($\varphi = 0.30$).

Each cell in Table 3 contains two values. The first uses as a reference the formula by Dodge and Metzner [37] (Eq. (37)), whereas the latter, between two brackets, refers to the formula of Anbarlooei et al. [38] (Eq. (39)). Both values are quite close to each other, which suggests that the effect of the turbulence model and the switch between the different viscosity models could be evaluated by referring to either of the literature correlations. Even for the reference Newtonian fluid, ($n = 1.0$), the turbulence model significantly affects the level of agreement between our RANS predictions and the literature formulas, the MAPE being $\approx 2.5\%$ with the SST and $\approx 7.5\%$ with the LB and the 2L. For the shear-thinning cases, the model with constant viscosity ($\mu = \rho/Re_\tau$) results in higher errors compared to using the Newtonian RANS model, and these errors increase as n decreases. In most models, the MAPE values range from $\approx 10.0\%$ to $\approx 30.0\%$, indicating the unfeasibility of neglecting shear-thinning effects. Regarding the effect of switching from the Newtonian RANS model to our approach, for $n = 0.8$, the MAPE remains unchanged with the SST, whereas it decreases with the LB and the 2L. Then, with all turbulence models, the deviation increases for $n = 0.6$ and even more for $n = 0.4$. The benefit of our approach depends on the turbulence model. With the LB and 2L models, a significant decrease in the MAPE was found compared to the Newtonian RANS model, whilst the situation is the opposite with the SST for $n = 0.6$ and 0.4. Considering all shear-thinning cases (final row, $n < 1.0$), the 2L model displayed the smallest MAPE, in line the previous findings obtained by reference to the DNS data.

Table 3
MAPE of the friction factor obtained from our simulations relative to the empirical correlations. Each cell presents two MAPE values: the first was calculated using the correlation by Dodge and Metzner [37] (Eq. 37) as reference, while the second, enclosed in brackets, was estimated using the correlation by Anbarlooei et al. [38] (Eq. 39). Each MAPE value was computed over $N = 10$ with Re_τ ranging from 323-2500, except for the last row, which considers 30 data points corresponding for all shear-thinning cases.

n	LB			2L			SST		
	Newt. RANS $\mu = \rho/\mathrm{Re}_\tau$	Newt. RANS Eq. (6)	Prop. app. Eq. (10)	Newt. RANS $\mu = \rho/\mathrm{Re}_\tau$	Newt. RANS Eq. (6)	Prop. app. Eq. (10)	Newt. RANS $\mu = \rho/\mathrm{Re}_\tau$	Newt. RANS Eq. (6)	Prop. app. Eq. (10)
1.0	7.1 (6.3)	7.1 (6.3)	–	7.8 (6.9)	7.8 (6.9)	–	2.5 (2.9)	2.5 (2.9)	–
0.8	9.6 (9.3)	1.7 (2.4)	1.1 (2.3)	10.4 (10.0)	1.6 (1.0)	1.7 (0.8)	2.1 (1.2)	2.6 (1.9)	2.5 (1.9)
0.6	16.4 (17.1)	12.3 (11.8)	9.1 (8.5)	17.3 (17.9)	9.4 (8.7)	5.0 (4.7)	6.5 (7.1)	4.0 (4.2)	4.5 (5.0)
0.4	34.7 (31.9)	24.0 (25.6)	14.0 (15.7)	35.8 (32.9)	13.9 (15.1)	6.3 (6.7)	23.3 (20.7)	16.7 (14.2)	20.3 (17.7)
<1.0	20.3 (19.4)	12.6 (13.3)	8.1 (8.8)	21.2 (16.9)	8.3 (8.2)	4.5 (4.0)	31.9 (9.7)	7.8 (6.8)	9.1 (8.2)

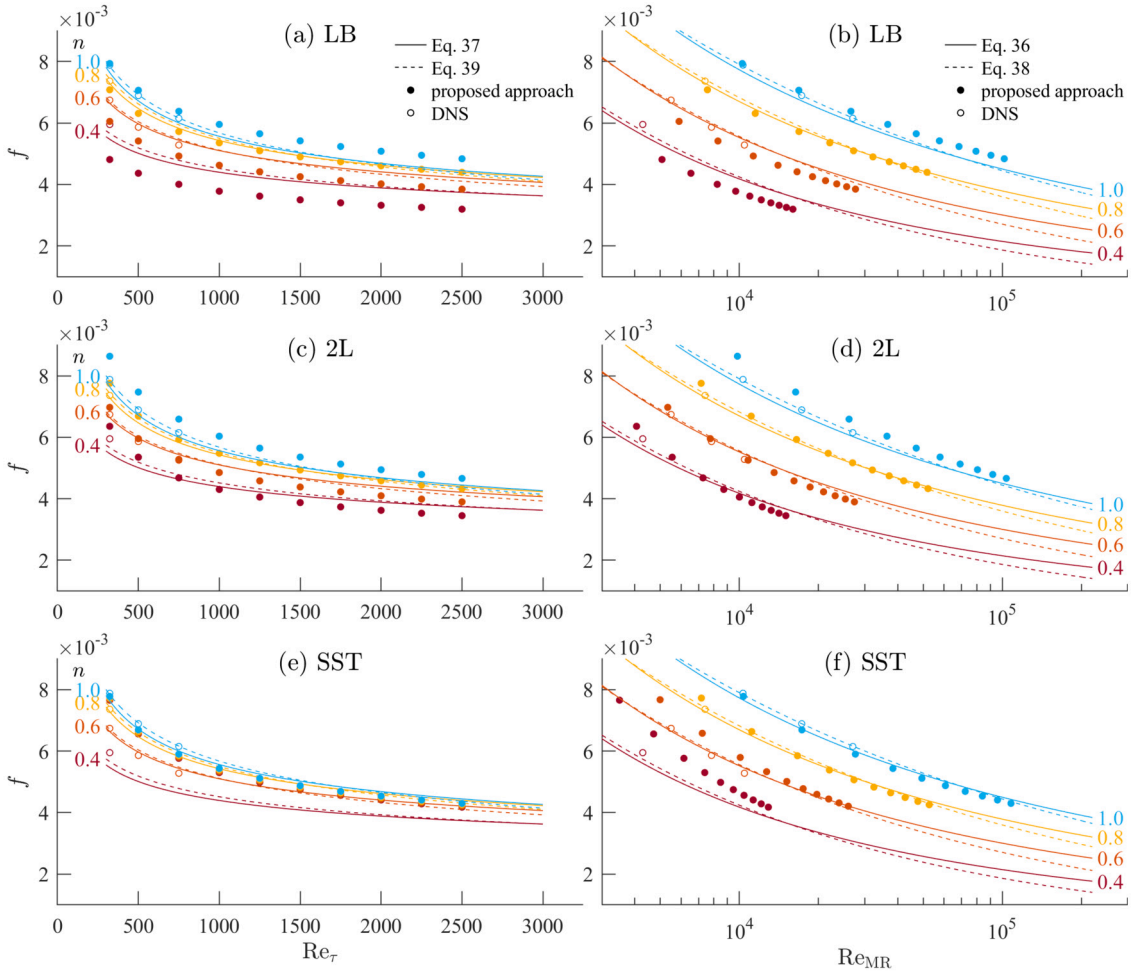

Fig. 5. Friction factors obtained at fixed $\varphi = 0.30$ and different combinations of n, Re_τ and turbulence model. Figures (a, c, e) are plotted as a function of Re_τ, whereas (b, d, f) are plotted as a function of $\mathrm{Re}_{\mathrm{MR}}$.

Finally, a qualitative assessment of the prediction accuracy of the frictional losses was obtained by referring to Fig. 5, which provides a comprehensive overview of all friction factors obtained from our simulations at $\varphi = 0.30$ (with the three turbulence models), as well as from the DNS data of Singh et al. [11,12] and the empirical correlations of Dodge and Metzner [37] and Anbarlooei et al. [38]. Particularly, the three plots on the left (Fig. 5 a-c-e) describe the friction factor as a function of the friction Reynolds number, Re_τ, whereas those on the right (Fig. 5 b-d-f) are in terms of the Reynolds number of Metzner and Reed, $\mathrm{Re}_{\mathrm{MR}}$. The visualization of the results is quite difficult in the curves on the left, hence, the figures on the right serve as support for discussion. The plots provide evidence that, for the flow conditions under investigation, the discrepancy between Eqs. (37) and (39) (or Eqs. (36) and (38)) is quite small except at very large $\mathrm{Re}_{\mathrm{MR}}$, which is in line with the MAPE values in Table 3. In general, all turbulence models are able to capture

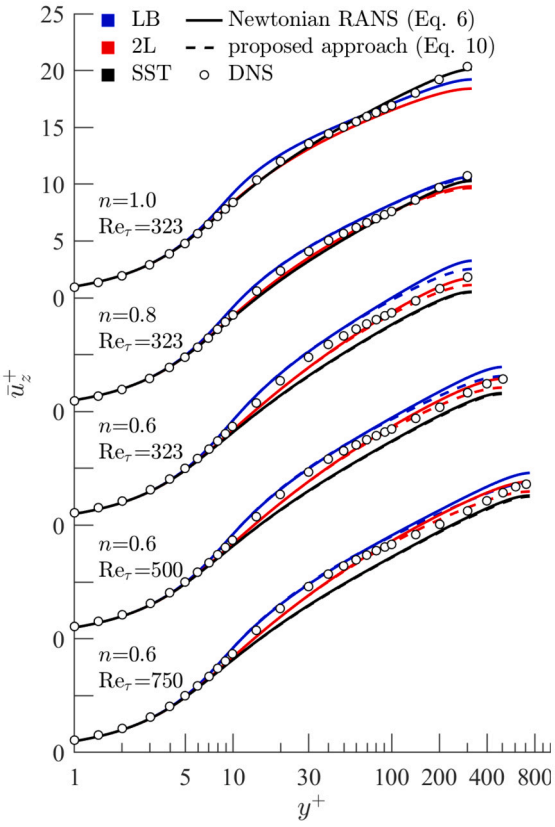

Fig. 6. Normalized profiles of the Reynolds averaged axial velocity for different combinations of n and Re_τ. The plots compare our simulation results with and without the viscosity limiter, as obtained from three turbulence models, and the DNS data from Singh et al. [11,12].

the effect of n and Re_τ (or $\mathrm{Re}_{\mathrm{MR}}$) on the frictional losses accurately from a qualitative point of view, and, in most cases, also from a quantitative perspective. Focusing on the results for shear-thinning fluids ($n < 1.0$), the LB model generally provides good predictions but underestimates frictional losses for $n = 0.60$ and $n = 0.40$ (Fig. 5a-b). The 2L model gives the closest agreement with the DNS data and frictional correlations, with very accurate predictions for $n = 0.6$ and 0.8, and a slight worsening for $n = 0.4$ (Fig. 5c-d). The SST model shows very good agreement for $n = 0.8$. For $n = 0.6$ the agreement improves as the Reynolds number increases, but for $n = 0.4$, the predictions are poor, especially at low Reynolds numbers (Fig. 5e-f).

5.4. Reynolds-averaged axial velocity

The results illustrating the normalized Reynolds-averaged axial-velocity profile for different combinations of n and Re_τ are presented in Fig. 6. The Reynolds-averaged axial velocity is normalized by u_τ and plotted as a function of y^+, in a logarithmic scale. Also for this variable, the effect of the turbulence model is significant.

First, the results will be analysed focusing on the effect of changing n for the same $\mathrm{Re}_\tau = 323$. The Newtonian fluid case ($n = 1$, upper block) serves as a reference for assessing the accuracy of tested turbulence models under standard conditions. For Newtonian fluids, SST demonstrates the closest agreement with the DNS data, whereas the LB and 2L models tend to underestimate the velocity in the core region. At $n = 0.8$ (second block from the top), all turbulence models agree with the DNS results, albeit with some disparities in the buffer layer. There is practically no difference between the Newtonian RANS model and our approach, except for the 2L solutions in the core region; in this case, in fact, applying $\varphi = 0.30$ slightly increases the distance of our CFD solution from the DNS data. Focusing the attention towards the case $n = 0.6$ and $\mathrm{Re}_\tau = 323$ (third block from the top), the LB model overestimates the velocity within the buffer and core regions, but the deviation is reduced with our approach. On the contrary, the SST model underestimates the mean velocity from the buffer layer towards the core, our approach providing no benefit over the Newtonian RANS formulation. On the contrary, using the 2L model, the Newtonian RANS model demonstrates the closest agreement with DNS data, whereas our approach results in a slight velocity underestimation within the core.

Afterwards, some considerations were made by considering the solutions for different Re_τ and the same $n = 0.6$ (last three blocks). Regardless of the value of Re_τ, the LB model with the original formulation ($\varphi = 0$) overpredicts the DNS data within the logarithmic layer and the core regions, whereas applying $\varphi = 0.30$ demonstrates improved results in the core region. The 2L model with the original formulation yields generally very good results, albeit with a slight deviation in the buffer layer. Conversely, the 2L model

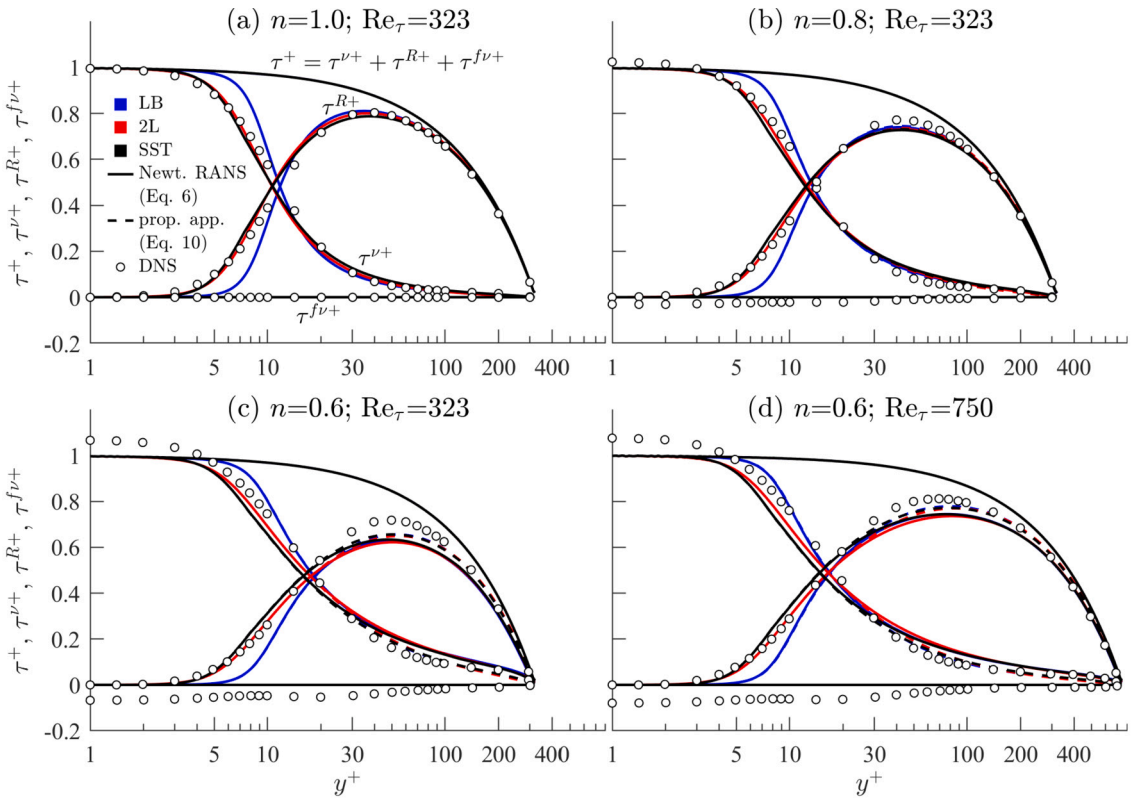

Fig. 7. Mean shear stress budget at different values of n and Re_τ. The plots compare our simulation results with and without the critical shear rate, as obtained from three turbulence models, and the DNS data from Singh et al. [11,12].

with $\varphi = 0.30$ tends to slightly underestimate the velocity in the core region. The SST model underestimates the Reynolds-averaged velocity data from the buffer layer towards the core region.

5.5. Reynolds-averaged shear-stress budget

Following Eq. (5b), the total Reynolds-averaged shear stress for non-Newtonian fluids is

$$\tau_{ij} = 2\bar{\mu}\bar{s}_{ij} - \rho\overline{u_i' u_j'} + 2\overline{\mu' s_{ij}'} \tag{42}$$

In pipe flows, using cylindrical coordinates and accounting for the axisymmetric behaviour of the Reynolds average flow field, the equation here above can be rearranged as

$$\tau_{rz}^+ = \tau_{rz}^{\nu+} + \tau_{rz}^{R+} + \tau_{rz}^{f\nu+} = \frac{r}{R} = 1 - \frac{y^+}{\mathrm{Re}_\tau} \tag{43}$$

where $\tau_{rz}^{\nu+}$, τ_{rz}^{R+} and $\tau_{rz}^{f\nu+}$ correspond to the three terms in Eq. (42), and they are called viscous stress, Reynolds stress, and turbulent viscous shear stress, the latter being referred to as the non-Newtonian shear stress in other works. In order to make them dimensionless, all shear stresses are normalized by the wall shear stress, τ_w. The linear dependency of τ_{rz} with r might be derived analytically from the Reynolds-averaged mass and momentum conservation equations, whereas the equality $r/R = 1 - y^+/\mathrm{Re}_\tau$ comes from Eq. (30) and the definition of y^+. To simplify the nomenclature, from this point onward the subscript rz is omitted. The values of $\tau^{\nu+}$ and τ^{R+} are numerically derived from the constitutive model for the stress tensor and the Boussinesq assumption, respectively.

$$\tau^{\nu+} = \frac{1}{\tau_w}\left[\bar{\mu}\left(-\frac{\mathrm{d}\bar{u}_z}{\mathrm{d}r}\right)\right] \tag{44}$$

$$\tau^{R+} = \frac{1}{\tau_w}\left[\mu_t\left(-\frac{\mathrm{d}\bar{u}_z}{\mathrm{d}r}\right)\right] \tag{45}$$

In the Newtonian RANS framework, $\tau_{rz}^{f\nu+}$ is not accounted for, thereby affecting the balance of the other two shear stresses.

The Reynolds-averaged shear-stress budget is depicted in Fig. 7 for different combinations of n and Re_τ. Specifically, the effect of n at fixed $\mathrm{Re}_\tau = 323$ is presented in Fig. 7a-c. The Newtonian fluid case is again utilized as a benchmark for assessing the accuracy of the turbulence models. Both the 2L and the SST results align very well with the DNS data for Newtonian flow, whereas the LB model

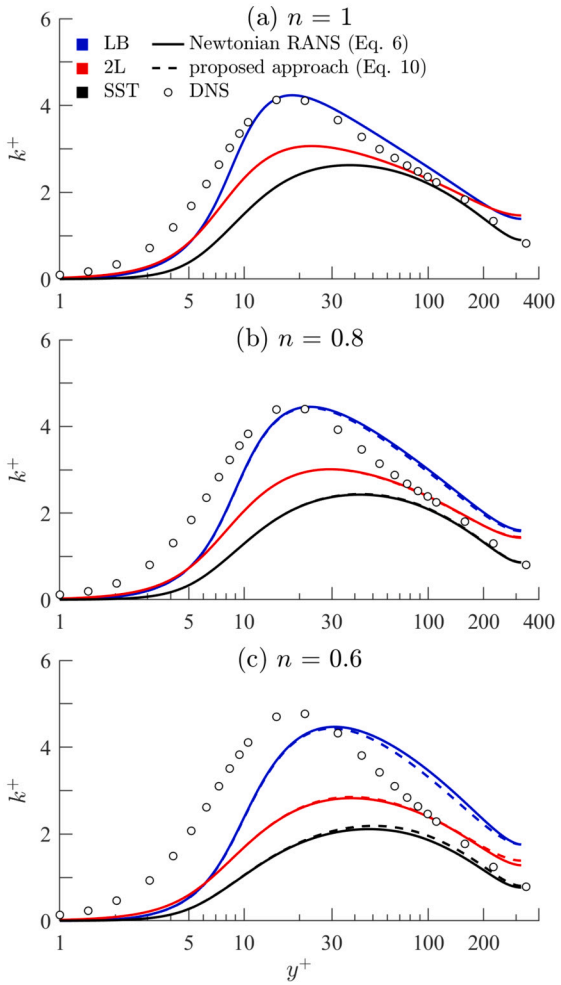

Fig. 8. Turbulent kinetic energy profiles at $\mathrm{Re}_\tau = 323$ and different values of n. The plots compare our simulation results, both with and without the critical shear rate, obtained using three turbulence models, against the DNS data from Singh et al. [11,12].

exhibits some deviation in the inner portion of the buffer layer (Fig. 7a). For $n = 0.8$, the LB model still deviates from the DNS results in the inner portion of the buffer layer, whereas the 2L and the SST solutions keep close to the literature data. For all turbulence models, the effect of introducing the logarithmic branch in the average apparent viscosity formula is not noticeable (Fig. 7.b). For $n = 0.6$ and $\mathrm{Re}_\tau = 323$, the DNS data indicate a more pronounced contribution of τ^{fv+}, affecting also the other components of the shear-stress budget. Compared to the Newtonian RANS formulation, our approach enhances the accuracy of the τ^{v+} predictions throughout the logarithmic layer and core region, and also slightly improves the estimation of τ^{R+} (Fig. 7.c), a tendency observed with all turbulence models, including the SST. The benefit persists at higher Re_τ (Fig. 7.d). Thus, adhering to the shear-stress budget, our approach not only improves the prediction of the apparent viscosity profile over the Newtonian RANS model, but it also enhances the accuracy of the estimation of τ^{v+} and τ^{R+} in the logarithmic layer and core region, compensating for the neglect of τ^{fv+}.

5.6. Turbulent kinetic energy

The results of turbulent kinetic energy k for various flow indices n and $\mathrm{Re}_\tau = 323$ are presented in Fig. 8, where the turbulent kinetic energy is normalized by u_τ^2 and plotted as a function of y^+, in a logarithmic scale. In the Newtonian fluid case ($n = 1$), accurate predictions of k are evident only with the LB model (Fig. 8.a), while other models underestimate the magnitude of k and overestimate the peak location. Within the Newtonian RANS framework, the solutions of the LB and 2L models are almost insensitive to the value of n; consequently, the high accuracy of the LB solution for $n = 1$ deteriorates for $n = 0.8$ and 0.6 (Fig. 8.b-c). On the other hand, the SST model predicts a lower peak k as n decreases, whilst the DNS data show an opposite trend. Transitioning from the Newtonian RANS framework to our approach produces only small changes to the k, depending on the turbulence model. The LB model shows a decrease in k from the peak toward the core region, whereas the SST model exhibits an increase around the peak, extending towards the core. Finally, all models indicate that increasing shear-thinning effects shift the k-peak location further from the wall. However, the final location from the wall is overestimated.

5.7. Production, transport and dissipation of k

Low-Reynolds-number turbulence models allow us to obtain detailed information of the terms in the transport equation of k close to the wall. In a purely viscous non-Newtonian fluid, the transport equation for k is:

$$\rho\bar{u}_j\frac{\partial k}{\partial x_j} = \mathcal{P} + \{\overbrace{\mathcal{T}+\Pi+\mathcal{D}+\mathcal{D}_{nn}+\xi_{nn}}^{T^k}\} - \rho\{\overbrace{\varepsilon+\chi_{nn}+\varepsilon_{nn}}^{\varepsilon^k}\} \tag{46}$$

where $\mathcal{P}$ is the production of k, T^k represents the total transport by grouping terms of a similar nature, and ε^k is the total dissipation rate, also grouping terms of a similar nature. The extra non-Newtonian terms are the turbulent viscous transport $\mathcal{D}_{nn}$, the mean-shear turbulent viscous transport ξ_{nn}, the mean-shear turbulent viscous dissipation χ_{nn}, and the turbulent viscous dissipation ε_{nn}. The definition of all terms on the right hand side of Eq. (46) can be examined in previous works [24,44,11]. For the Newtonian fluid case, Eq. (46) is reduced to:

$$\rho\bar{u}_j\frac{\partial k}{\partial x_j} = \mathcal{P} + \{\overbrace{\mathcal{T}+\Pi+\mathcal{D}}^{T^k}\} - \rho\overbrace{\{\varepsilon\}}^{\varepsilon^k} \tag{47}$$

which is the formulation employed in our approach, as previously seen in Eq. (15) in Section 2. Additionally, in fully-developed turbulent pipe flows, the term in the left side of Eq. (15) (or Eq. (46)) is equal to zero. We will now analyse the redistribution of the different terms in the right hand side of Eq. (47) for shear-thinning fluids. To this aim, profiles of the normalized components in Eq. (47), $\mathcal{P}^+$, T^{k^+} and ε^{k^+}, are examined for different values of n with $\mathrm{Re}_\tau = 323$ fixed, as shown in Fig. 9.a-c. The terms are normalized by $\rho u_\tau^4/\nu_w$ and plotted as a function of y^+ on a logarithmic scale. Firstly, it was noticed that the differences between our approach and the Newtonian RANS model were negligible, suggesting that the introduction of the logarithmic function in the average apparent viscosity model does not significantly affect the terms in the k equation. This was interpreted as a consequence of the fact that, although T^{k^+} and ε^{k^+} depend on the Reynolds-averaged apparent viscosity, their values are quite small in the core region of the pipe, where the influence of introducing φ is more pronounced. Hence, only the curves obtained with our approach are shown in Fig. 9.a-c. As a basis for comparison, the DNS results of Singh et al. [11] for the same dimensionless variables $\mathcal{P}^+$ (unfilled circles), T^{k^+} (unfilled squares) and ε^{k^+} (unfilled diamonds), and the same values of n, are also presented. Note that, however, Singh et al. [11] obtained $\mathcal{P}^+$, T^{k^+} and ε^{k^+} through the generalized Eq. (46), and not through the simplified Eq. (47).

The sum of $\mathcal{P}^+$, T^{k^+} and ε^{k^+} is zero along all values of y^+, as shown by the horizontal grey line. It is observed that our simplification of excluding the non-Newtonian terms from Eq. (46) does not affect the consistency between our results and the DNS data. Across all RANS models, $\mathcal{P}^+$ increases as n increases in the region where $y^+ \lesssim 23$. For LB and 2L, $\mathcal{P}^+$ slightly decreases with increasing n for $y^+ \gtrsim 23$. Similarly, T^{k^+} increases in magnitude as n increases for $y^+ \lesssim 23$ across all RANS models, while it slightly decreases in magnitude for $y^+ \gtrsim 23$ in the LB model. Additionally, for LB and 2L, ε^{k^+} increases in magnitude as n increases for $y^+ \lesssim 23$. The SST model exhibits this trend across all y^+. Discrepancies with the DNS data are noted, even in the Newtonian case, in aspects such as the dissipation-rate shape in the $y^+ \lesssim 10$ region the magnitude of T^{k^+} in all models. Overall, the tested low-Reynolds-number turbulence models appear to effectively capture the influence of n on the terms in the transport equation of k close to the wall.

6. Discussion and perspectives

6.1. Behaviour of the average apparent viscosity at the pipe centreline

It has been widely discussed that Newtonian RANS models suffer from the issue of the average apparent viscosity tending to infinity in the pipe centreline. Although our approach does not solve this issue, it makes $\bar{\mu}$ approach infinity at a reduced rate, as is clearly seen in Figs. 3 and 4.

In order to prevent the average apparent viscosity to tend to infinity, the simplest possible option would be to introduce an upper threshold, $\bar{\mu}_{\max}$, which is activated when the average shear rate is below to another limit in the core region, $\bar{\dot{\gamma}}_{c,2}$. In this way, the apparent viscosity function would change as follows

$$\bar{\mu}(\bar{\dot{\gamma}}) = \begin{cases} \bar{\mu}_{\max} & \text{for } \bar{\dot{\gamma}} < \bar{\dot{\gamma}}_{c,2} \\ a\ln\bar{\dot{\gamma}} + b & \text{for } \bar{\dot{\gamma}}_{c,2} \le \bar{\dot{\gamma}} < \bar{\dot{\gamma}}_c \\ m\bar{\dot{\gamma}}^{n-1} & \text{for } \bar{\dot{\gamma}} \ge \bar{\dot{\gamma}}_c \end{cases} \tag{48}$$

which makes it evident that the number of coefficients of the model has increased to four, as they are m, n, $\bar{\dot{\gamma}}_c$, and $\bar{\dot{\gamma}}_{c,2}$. Having already established that m and n are obtained from the rheological characterization of the fluid, $\bar{\dot{\gamma}}_c$ and $\bar{\dot{\gamma}}_{c,2}$ must be obtained from calibration. In order to explore the actual effectiveness of Eq. (48), pipe flow cases were run in which $\bar{\dot{\gamma}}_{c,2}$ was varied, as shown in Fig. 10. Specifically, we considered the same test cases presented in Fig. 3 using the LB turbulence model. The critical shear rate, $\bar{\dot{\gamma}}_c$ was kept as $0.30\bar{\dot{\gamma}}_w$, based on the previous calibration of the three-parameter function. For formal coherence with $\bar{\dot{\gamma}}_c$, also $\bar{\dot{\gamma}}_{c,2}$ was expressed as a fraction of the shear rate at the wall, $\bar{\dot{\gamma}}_{c,2} = \psi\bar{\dot{\gamma}}_w$, although this formulation is somehow artificial, since $\bar{\dot{\gamma}}_{c,2}$ affects the core region of pipe flow. Fig. 3 shows the curves corresponding to $\psi = 0.0010$ (solid blue line), $\psi = 0.0020$ (dashed blue line), ψ

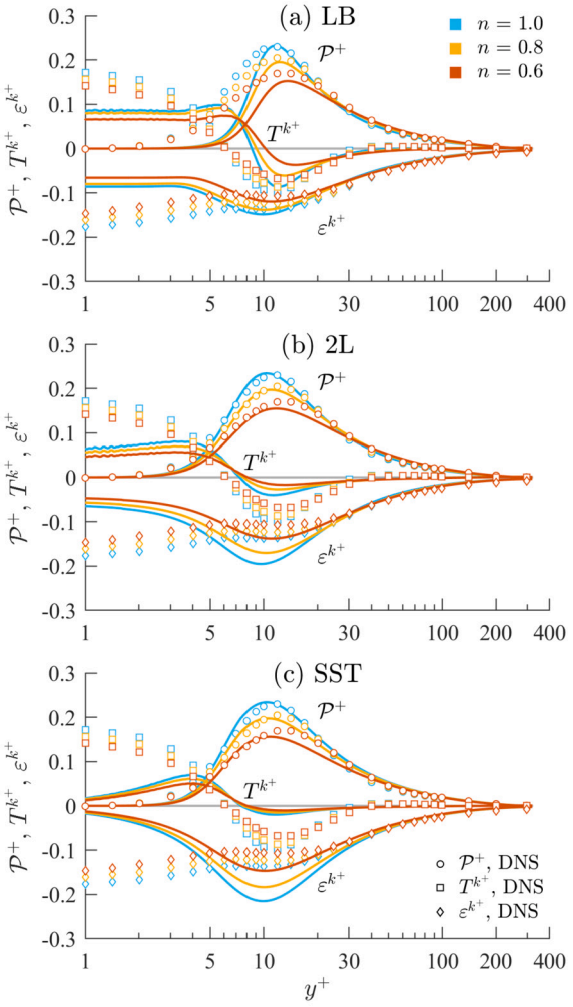

Fig. 9. Profiles of production, total transport and total dissipation rate at $\mathrm{Re}_\tau = 323$ and different values of n. The results of each turbulence model are contrasted with the DNS data from Singh et al. [11,12].

$= 0.0030$ (dash-dotted blue line), and $\psi = 0.0050$ (dotted blue line), plus the reference case $\psi = 0.0000$ (solid black line) which corresponds to our approach with no maximum viscosity limit activated. This time, y/R was preferred to y^+ in the horizontal axis for a better visualisation of the results. For the tested cases, applying a value of $\bar{\mu}_{\max}$ through $\bar{\dot{\gamma}}_{c,2}$ proved to be effective in removing the sharp increase of average apparent viscosity near the centreline. The choice of an optimal value of ψ in an absolute sense was not possible. The overall behaviour of the curves suggested that, for $n = 0.6$, appropriate values for ψ were 0.0050, 0.0020 and 0.0010 for $\mathrm{Re}_\tau = 323$, 500 and 750, respectively. All of these values limit the average viscosity at $y/R \gtrsim 0.85$.

Although Eq. (48) prevents the apparent viscosity from increasing indefinitely as the pipe axis is approached, it makes the model more complex and more difficult-to-calibrate, reducing its practical usability which is precisely its strength. Also, the introduction of ψ was found to have minimal or even undetectable influence on parameters other than the Reynolds-averaged apparent viscosity profile in the pipe axis. Based on these considerations, our preference is for the single parameter function (Eq. (10)).

6.2. An alternative formulation using the Reynolds-averaged apparent viscosity function of Gavrilov and Rudyak [14]

In order to further assess the capability of our approach, we investigated the effect of replacing Eq. (10) with the average apparent viscosity function of Gavrilov and Rudyak [14], which reads as follows,

$$\bar{\dot{\gamma}}^2 = 2\bar{s}_{ij}\bar{s}_{ij} + \rho\varepsilon/\bar{\mu}, \quad \bar{\mu} = m(\bar{\dot{\gamma}}^2)^{\frac{n-1}{2}} \tag{49}$$

Note that, in Eq. (49), the relation between $\bar{\mu}$ and $\bar{\dot{\gamma}}$ is implicit, and it also involves the turbulent dissipation rate, ε. This might suggest that, compared to Eq. (10), Eq. (49) would be more challenging, or slower, to converge, even if the authors recommended a two-step method that efficiently integrates the implicit function into the main solution algorithm. Note also that our goal here is not to make a comparison between our approach and the non-Newtonian RANS model of Gavrilov and Rudyak [14], which keeps the

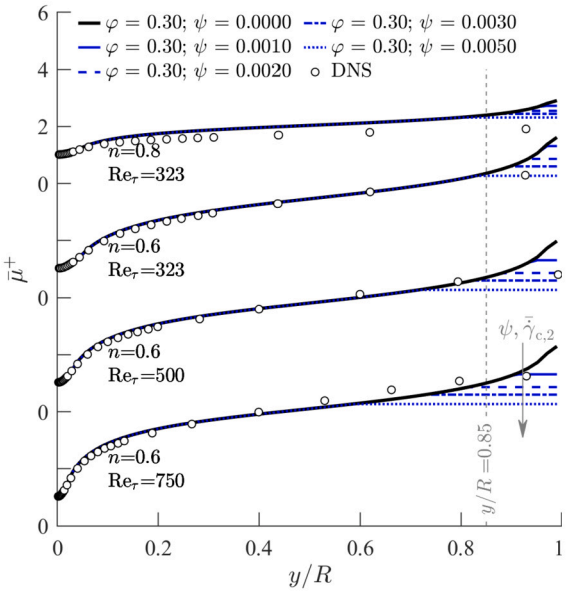

Fig. 10. The effect of the maximum average apparent viscosity in the average apparent viscosity function (Eq. 48) for the LB model. The viscosity profiles are compared with DNS data from Singh et al. [11,12].

Table 4
Number of iterations and CPU time to reach convergence for different turbulence models and average apparent viscosity formulations. The number values are the average over all combinations of n and Re_τ, plus or minus the standard deviations. The simulations were performed on a computer with Inter core i9-11900 with 32 GB RAM, using a single core.

Turbulence model	Model for $\bar{\mu}$	Iterations	CPU time (s)
LB	Newtonian RANS (Eq. 6)	4714 ± 1717	4 ± 1
LB	proposed approach (Eq. 10) with $\varphi = 0.30$	4421 ± 2097	5 ± 2
LB	Gavrilov and Rudyak (Eq. 49)	4391 ± 1654	6 ± 3
2L	Newtonian RANS (Eq. 6)	≤ 1000	≈ 1
2L	proposed approach (Eq. 10) with $\varphi = 0.30$	≤ 1000	≈ 1
2L	Gavrilov and Rudyak (Eq. 49)	9700 ± 1643	15 ± 4
SST	Newtonian RANS (Eq. 6)	1274 ± 224	≈ 2
SST	proposed approach (Eq. 10) with $\varphi = 0.30$	1461 ± 310	≈ 2
SST	Gavrilov and Rudyak (Eq. 49)	1497 ± 290	3 ± 1

$\overline{\mu' s'_{ij}}$ term in the momentum equation, and uses a modified formulation of the ζ-f turbulent model which includes correlation terms specific to non-Newtonian fluids. Instead, our goal is simply to show the strengths and weaknesses of our approach by exploring the effect of changing the apparent viscosity function.

When comparing the two functions, we considered all solution outputs presented in Section 5. For reasons of space and opportunity, we will present and discuss only the average apparent viscosity and average axial velocity profiles, which led to the most interesting findings. The normalized average apparent viscosity profiles are shown in Fig. 11 where, specifically, the predictions using Eq. (49) (dotted lines) are compared against our approach (segmented lines) and the DNS data from [11,12] (unfilled circles). As usual, the results are provided for three turbulence models (LB, 2L, SST). It is immediately evident that incorporating Eq. (49) into the Newtonian framework solves the issue of $\bar{\mu}$ tending to infinity at the pipe centreline. Additionally, Eq. (49) does not depend on any calibration parameter, whether our function (Eq. (10)) requires determining the appropriate value of $\bar{\gamma}_c$. At the same time, the level of accuracy of the model with Eq. (49) depends on n. When shear-thinning effects are weak ($n = 0.8$), Eq. (49) provides very good agreement with the DNS data, whereas our approach tends to overestimate the average apparent viscosity from the buffer layer toward the core region, as previously discussed. Conversely, when n is reduced to 0.6, overall our approach performs better than Eq. (49), which underestimates the average apparent viscosity in both the buffer and log layers but accurately captures its profile in the core region. Additionally, Eq. (49) displays sensitivity to the choice of the turbulence model in the core region.

When looking at the averaged axial velocity profiles in Fig. 12, there is no clear benefit of using Eq. (49) instead of our apparent viscosity function (Eq. (10)), as the degree of agreement with the DNS data is mainly dependent on the turbulence model. With the LB turbulence model, the predictions of Eq. (49) are more accurate than those of our approach, whereas an opposite situation is observed with the 2L turbulence model. Finally, with the SST turbulence model switching from Eq. (10) to (49) produces a minimal variation.

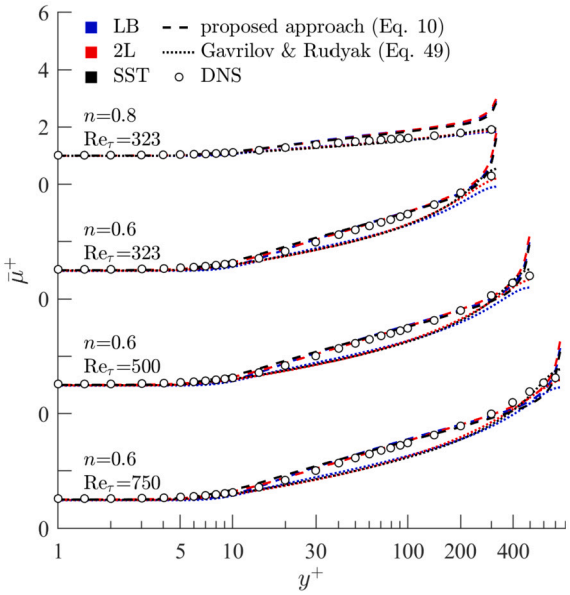

Fig. 11. Normalized profiles of the Reynolds-averaged apparent viscosity for different combinations of n and Re_τ. The plots compare our calibrated approach and the prediction obtained through Eq. 49 [14], as obtained from three turbulence models, and the reference DNS data from Singh et al. [11,12].

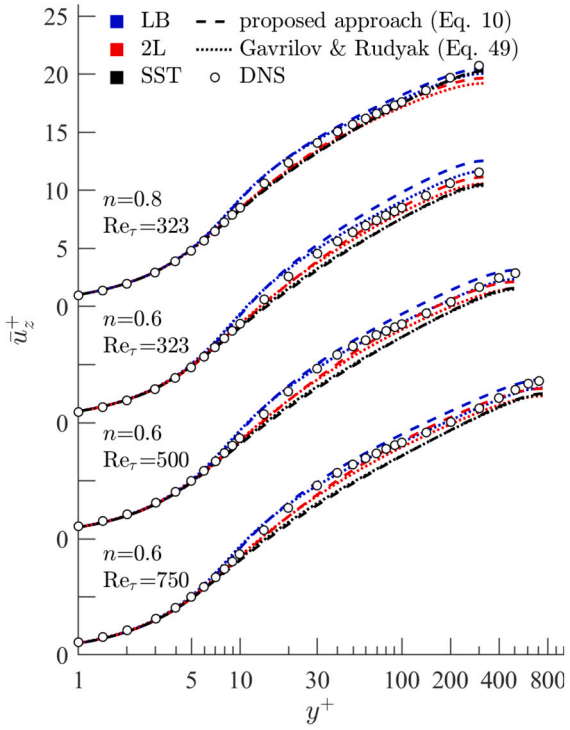

Fig. 12. Normalized profiles of the Reynolds averaged axial velocity for different combinations of n and Re_τ. The plots compare our calibrated approach and the prediction obtained through Eq. 49 [14], as obtained from three turbulence models, and the reference DNS data from Singh et al. [11,12].

Finally, we compared the two average apparent viscosity formulations in terms of their numerical performance, that is, ease of convergence and computational cost. The results only provide a rough indication and should be interpreted with care for several reasons. Firstly, the numerical performance of each formulation can be significantly dependent on the architecture of the CFD platform, as well as on the user-defined implementation. Secondly, the small computational cost of the pipe flow simulations using the fully developed solver makes such a case not so relevant for its evaluation. Thirdly, as already noticed, no comparison was made against the literature model of Gavrilov and Rudyak [14], but rather against a simpler formulation using Gavrilov and Rudyak's correlation

for the average apparent viscosity. With these premises in mind, we conducted a thorough comparison of the two $\bar{\mu}$ formulations for all combinations of n and Re_τ and the three turbulence models, keeping the same initial conditions and under-relaxation parameters. For the sake of a better assessment of the numerical performance of the models, we added as a third term of comparison the classical Newtonian RANS formulation with Eq. (6). In almost all the 360 runs, the threshold value of 10^{-6} was reached for all variables. Even in the few runs where this was not the case for some variables, typically k and ϵ, the CFD solution was smooth and appeared consistent from both qualitative and quantitative perspectives. Nonetheless, we chose to disregard those cases in the subsequent analysis. Table 4 shows the number of iterations and the approximate CPU time to attain a converged solution according to the criterion above. The numerical values are the mean over the combinations of n and Re_τ, plus or minus the standard deviation. The influence of the turbulence model is evident also in terms of the computational burden. For the same turbulence model, the Gavrilov and Rudyak's correlation for the average apparent viscosity (Eq. (49)) requires longer simulation times than our approach (Eq. (10)), which, in turn, is slower to solve than the standard Newtonian RANS approach (Eq. (6)). The results with the 2L turbulence model are particularly noticeable as, in this case, the use of Eq. (49) amplifies very significantly both the number of iterations to reach the desired threshold convergence criterion and the CPU time. Finding the causes of this behaviour compared to the two other turbulence models requires further investigation, and possibly the difference could be reduced by modifying some of the solution settings of the code. Nonetheless, that would not be the scope of the short analysis presented here. Instead, we just wanted to show that, even for a simple straight pipe flow simulated with the fully developed solver, incorporating Eq. (49) within the Newtonian RANS framework might produce numerical challenges. It is fully reasonable to expect that such challenges will further increase when the model with Eq. (49) is applied to more complex geometries, and even more so when a full non-Newtonian RANS model is employed. This strengthens the conviction that our approach could reveal its value in the simulation of more complex geometries, as discussed in the next section.

6.3. Considerations on the applicability to more complex flows

Whilst the model has been formulated to be as general as possible, as our aim was to develop a tool applicable to complex geometries, its practical application faces a number of challenges. This short section is mostly to be viewed as an outline of open problems, rather than a statement of results.

A first issue is the characterization of the critical shear rate, $\overline{\dot{\gamma}}_c$. In this study, we expressed $\overline{\dot{\gamma}}_c$ as a function of the value of the shear rate at the pipe wall, $\overline{\dot{\gamma}}_w$, recommending $\overline{\dot{\gamma}}_c = 0.30\overline{\dot{\gamma}}_w$ based on the overall agreement with DNS data. However, this approach does not seem appropriate, or, at least, easy to implement, for other domain geometries, since the identification of $\overline{\dot{\gamma}}_w$ for a certain computation cell might not be straightforward. Although algorithms exist for the efficient evaluation of the nearest wall node to a given computational cell, whether expressing the critical shear rate as a fraction of the shear rate at the nearest wall would be appropriate or not is a question that does not have an obvious answer (nor, of course, whether the proportionality law $\overline{\dot{\gamma}}_c = 0.30\overline{\dot{\gamma}}_w$ would remain reasonable). Hence, further research is needed to determine a suitable criterion for evaluating $\overline{\dot{\gamma}}_c$ for arbitrary flows.

A second issue is the availability of data to validate the model. Experimental testing of power-law fluid flows in complex geometries has been reported, including pipe bends [45,46], as well as various types of valves and pipe fittings [45,47,48]. However, in all aforementioned studies, only the pressure drop and related parameters have been measured, which are not enough to provide a deep evaluation of our approach in absolute terms and compared to others. This certifies the difficulties in achieving a comprehensive and highly accurate experimental characterization of the turbulent flow of power-law fluids, strengthening the conviction that only DNS can provide the level of insight required for the validation of our RANS formulation and similar ones. Unfortunately, to the best of our knowledge, no DNS study has been published concerning the transport of power-law fluids in other geometries than straight pipes. Even the few published numerical investigations on pipe bends and fittings using RANS models were not of great help, since the relevant information on the used models was not fully disclosed [45,46,49]. Additionally, the validation of the simulation results was either absent or limited to pressure drop measurements.

In conclusion, although our proposed RANS approach, as well as the alternative ones, could be applied to arbitrary flows, a criterion or guideline for deciding the critical shear rate is missing. Additionally, the capability of the approach could be verified through the assessment of the physical soundness of the solution, but no exhaustive quantitative validation is possible due to the lack of adequate data for comparison. Having said that, and also on the basis of the results in Table 4, we are convinced that our approach could be numerically more efficient compared to the available non-Newtonian RANS model due to its mathematical simplicity. At present, however, this remains a reasonable speculation rather than established evidence.

7. Conclusions

In this study, we propose a simple, and efficient methodology for simulating turbulent flow of power-law shear-thinning fluids. The idea was to incorporate within the Newtonian RANS framework, which neglect the apparent viscosity fluctuations and employ turbulence models developed for Newtonian fluids, a modified average apparent viscosity model (Eq. (10)). The main findings are as follows:

- The modification of the average apparent viscosity model by introducing the logarithmic branch mostly affects the central region of the pipe flow, characterized by low shear rates. The change improves significantly the prediction of the Reynolds-averaged apparent viscosity profile, $\bar{\mu}$, which, using the standard Newtonian, RANS-based framework, was strongly overestimated. A good agreement with the $\bar{\mu}$ profile obtained by DNS was achieved by setting the "critical shear rate" equal to 30% of the value at the wall. This threshold appears to be a reasonable choice for different combinations of n and Re_τ.

- Our approach does not prevent the Reynolds averaged apparent viscosity going to infinity at the pipe axis, which is a well known limitation of Newtonian RANS models. However, the rate of increase of the Reynolds averaged apparent viscosity is slowed down compared to a standard Newtonian RANS model. Two strategies have been presented to fully resolve the issue, but none of them is free from criticism. The former consists in further modifying the Reynolds averaged apparent viscosity model imposing a maximum constant value at very low shear rates, which, however, introduces a second, difficult-to-decide, calibration parameter. The latter consists in replacing our Reynolds averaged apparent viscosity model with the one proposed by Gavrilov and Rudyak [14] in the context of a more complex non-Newtonian RANS framework, which, however, is implicit and increases the simulation time.
- The modification to the average apparent viscosity model improves significantly the $\bar{\mu}$ profile and its effect on the friction factor could be at times important, depending on the flow conditions and on the used turbulence model. It also slightly enhances the estimation of the viscous and Reynolds stress in the logarithmic and core regions of the pipe flow. Conversely, it has no impact on other flow variables like the average shear rate, the turbulent kinetic energy, and its energy budget (production, transport and dissipation).
- The choice of the turbulence model significantly affects all fluid-dynamic variables subject to investigation, except possibly for the $\bar{\mu}$ profile. Using one turbulence model instead of another affects not only the accuracy of the predictions, but also the benefit brought by the change to the average apparent viscosity model. Among the three turbulence models considered (LB, 2L, and SST), none is the best in an absolute sense, that is, producing the highest accuracy for all flow variables and flow conditions.
- Whilst bearing in mind the previous point, our preference is for the LB turbulence model. Although this model fails in correctly predicting the decay of the Reynolds-averaged shear rate and in the viscous-stress for the buffer region, it is the one model which produces the correct levels of turbulent kinetic energy (but not the effect of the fluid rheology on the location of the maximum turbulent kinetic energy). With the LB turbulence model, the improvement brought by the change in the average apparent viscosity model is obvious in terms of the friction factor, and, to a lesser extent, also on the Reynolds-averaged velocity profile.

Our approach represents a practical method to improve the accuracy of the CFD prediction of turbulent transport of shear-thinning power-law fluids within the Newtonian RANS framework. We proved that, for fully developed pipe flow, modifying the average apparent viscosity model as Eq. (10) is an effective way to keep the model simple whilst compensating for the approximations made. Our approach was conceived as a practical tool for simulating complex geometries, providing engineers with useful information on the flow that cannot be obtained through DNS simulations or laboratory experiments. At the moment, we were not able to test our approach for complex geometries of engineering interest, mainly because of the lack of adequate data for comparison. However, the findings obtained here for straight pipes strengthen the conviction that our approach could be a valid, and possibly more effective, alternative to existing ones, owing to its simple mathematical structure that translates into robustness and efficient numerical solution.

CRediT authorship contribution statement

J.I. Soto: Writing – review & editing, Writing – original draft, Validation, Software, Project administration, Methodology, Investigation, Funding acquisition, Formal analysis, Data curation, Conceptualization. **G.V. Messa:** Writing – review & editing, Writing – original draft, Supervision, Software, Methodology, Formal analysis, Conceptualization. **M.R. Malin:** Writing – review & editing, Software, Methodology. **W. Brevis:** Writing – review & editing, Supervision, Conceptualization.

Declaration of competing interest

The authors declare that they have no known competing financial interests or personal relationships that could have appeared to influence the work reported in this paper.

Acknowledgements

This work was supported by the Agencia Nacional de Investigación y Desarrollo (ANID, Chile) through the National Doctoral Scholarship / 2020-21201843.

Data availability

Data will be made available on request.

References

[1] L. Pullum, D.V. Boger, F. Sofra, Hydraulic mineral waste transport and storage, Annu. Rev. Fluid Mech. 50 (1) (2018) 157–185, https://doi.org/10.1146/annurev-fluid-122316-045027.

[2] A.K. Thota Radhakrishnan, J.B. van Lier, F.H. Clemens, Rheological characterisation of concentrated domestic slurry, Water Res. 141 (2018) 235–250, https://doi.org/10.1016/j.watres.2018.04.064.

[3] G.K. Auernhammer, S. Fataei, M.A. Haustein, H.P. Patel, R. Schwarze, E. Secrieru, V. Mechtcherine, Transparent model concrete with tunable rheology for investigating flow and particle-migration during transport in pipes, Mater. Des. 193 (2020) 108673, https://doi.org/10.1016/j.matdes.2020.108673.

[4] D.V. Boger, Rheology of slurries and environmental impacts in the mining industry, Annu. Rev. Chem. Biomol. Eng. 4 (2013) 239–257, https://doi.org/10.1146/annurev-chembioeng-061312-103347.

[5] R.B. Bird, R.C. Armstrong, O. Hassager, Dynamics of Polymeric Liquids, John Wiley & Sons, New York, Chichester, Brisbane, Toronto, Singapore, 1987.

[6] R.P. Chhabra, J. Richardson, Non-Newtonian Flow and Applied Rheology, Elsevier, 2008, https://linkinghub.elsevier.com/retrieve/pii/B9780750685320X00017.

[7] J. Singh, M. Rudman, H.M. Blackburn, A. Chryss, L. Pullum, L.J. Graham, The importance of rheology characterization in predicting turbulent pipe flow of generalized Newtonian fluids, J. Non-Newton. Fluid Mech. 232 (2016) 11–21, https://doi.org/10.1016/j.jnnfm.2016.03.013.

[8] J. Singh, M. Rudman, H.M. Blackburn, The effect of yield stress on pipe flow turbulence for generalised Newtonian fluids, J. Non-Newton. Fluid Mech. 249 (2017) 53–62, https://doi.org/10.1016/j.jnnfm.2017.09.007.

[9] A. Lugarini, A.T. Franco, The isolated effect of yield stress in viscoplastic turbulent flow, Phys. Fluids 36 (11) (2024) 115131, https://doi.org/10.1063/5.0234499.

[10] A.A. Gavrilov, V.Y. Rudyak, Direct numerical simulation of the turbulent flows of power-law fluids in a circular pipe, Thermophys. Aeromech. 23 (4) (2016) 473–486, https://doi.org/10.1134/S0869864316040016.

[11] J. Singh, M. Rudman, H.M. Blackburn, The influence of shear-dependent rheology on turbulent pipe flow, J. Fluid Mech. 822 (2017) 848–879, https://doi.org/10.1017/jfm.2017.296.

[12] J. Singh, M. Rudman, H.M. Blackburn, Reynolds number effects in pipe flow turbulence of generalized Newtonian fluids, Phys. Rev. Fluids 3 (9) (sep 2018), https://doi.org/10.1103/PhysRevFluids.3.094607.

[13] D.O. Cruz, F.T. Pinho, Turbulent pipe flow predictions with a low Reynolds number k-ϵ model for drag reducing fluids, J. Non-Newton. Fluid Mech. 114 (2–3) (2003) 109–148, https://doi.org/10.1016/S0377-0257(03)00119-8.

[14] A.A. Gavrilov, V.Y. Rudyak, Reynolds-averaged modeling of turbulent flows of power-law fluids, J. Non-Newton. Fluid Mech. 227 (2016) 45–55, https://doi.org/10.1016/j.jnnfm.2015.11.006.

[15] S. Lovato, G. Keetels, S. Toxopeus, J. Settels, An eddy-viscosity model for turbulent flows of Herschel–Bulkley fluids, J. Non-Newton. Fluid Mech. 301 (2022) 104729, https://doi.org/10.1016/j.jnnfm.2021.104729.

[16] M.R. Malin, Turbulent pipe flow of power-law fluids, Int. Commun. Heat Mass Transf. 24 (7) (1997) 977–988, https://doi.org/10.1016/S0735-1933(97)00083-3.

[17] V.C. Patel, W. Rodi, G. Scheuerer, Turbulence models for near-wall and low Reynolds number flows — a review, AIAA J. 23 (9) (1985) 1308–1319, https://doi.org/10.2514/3.9086.

[18] R. Sawko, Mathematical and Computational Methods of non-Newtonian, Multiphase Flows, PhD Thesis, School of Engineering, Cranfield University, Cranfield, UK, 2012, http://dspace.lib.cranfield.ac.uk/handle/1826/7264.

[19] D. Mehta, A.K. Thota Radhakrishnan, J.B. van Lier, F.H. Clemens, Assessment of numerical methods for estimating the wall shear stress in turbulent Herschel–Bulkley slurries in circular pipes, J. Hydraul. Res. 59 (2) (2021) 196–213, https://doi.org/10.1080/00221686.2020.1744751.

[20] B.K. Yusufi, Z. Kapelan, D. Mehta, Rheology-based wall function approach for wall-bounded turbulent flows of Herschel–Bulkley fluids, Phys. Fluids 36 (2) (2024), https://doi.org/10.1063/5.0180663.

[21] M.R. Malin, Turbulent pipe flow of Herschel-Bulkley fluids, Int. Commun. Heat Mass Transf. 25 (3) (1998) 321–330, https://doi.org/10.1016/S0735-1933(98)00019-0.

[22] D. Mehta, A.K.T. Radhakrishnan, J. van Lier, F. Clemens, A wall boundary condition for the simulation of a turbulent non-Newtonian domestic slurry in pipes, Water (Switzerland) 10 (2) (2018) 1–22, https://doi.org/10.3390/w10020124.

[23] B. Launder, D. Spalding, The numerical computation of turbulent flows, Comput. Methods Appl. Mech. Eng. 3 (2) (1974) 269–289, https://doi.org/10.1016/0045-7825(74)90029-2, arXiv:1204.1280.

[24] F. Pinho, A GNF framework for turbulent flow models of drag reducing fluids and proposal for a k–ϵ type closure, J. Non-Newton. Fluid Mech. 114 (2–3) (2003) 149–184, https://doi.org/10.1016/S0377-0257(03)00120-4.

[25] E. Amani, A. Ahmadpour, M.J. Aghajari, Large-eddy simulation of turbulent non-Newtonian flows: a comparison with state-of-the-art RANS closures, Int. J. Heat Fluid Flow 99 (November 2022) (2023) 109076, https://doi.org/10.1016/j.ijheatfluidflow.2022.109076.

[26] K. Hanjalić, M. Popovac, M. Hadžiabdić, A robust near-wall elliptic-relaxation eddy-viscosity turbulence model for CFD, Int. J. Heat Fluid Flow 25 (6) (2004) 1047–1051, https://doi.org/10.1016/j.ijheatfluidflow.2004.07.005.

[27] F.R. Menter, Improved two equation k-ω, Turbul. Models Aerodyn. Flows (1992).

[28] M. Taghvaei, E. Amani, Wall-modeled large-eddy simulation of turbulent non-Newtonian power-law fluid flows, J. Non-Newton. Fluid Mech. 322 (2023) 105136, https://doi.org/10.1016/j.jnnfm.2023.105136.

[29] A.V. Shenoy, D.R. Saini, A new velocity profile model for turbulent pipe-flow of power-law fluids, Can. J. Chem. Eng. 60 (5) (1982) 694–696, https://doi.org/10.1002/cjce.5450600519.

[30] M.T. Madhav, M.R. Malin, The numerical simulation of fully developed duct flows, Appl. Math. Model. 21 (8) (1997) 503–507, https://doi.org/10.1016/S0307-904X(97)00041-3.

[31] M.R. Malin, The turbulent flow of Bingham plactic fluids in smooth circular tubes, Int. Commun. Heat Mass Transf. 24 (6) (1997) 793–804, https://doi.org/10.1016/S0735-1933(97)00066-3.

[32] C. Lambride, A. Syrakos, G.C. Georgiou, Entrance length estimates for flows of power-law fluids in pipes and channels, J. Non-Newton. Fluid Mech. 317 (April 2023) 105056, https://doi.org/10.1016/j.jnnfm.2023.105056.

[33] D.T. Karahan, D. Ranjan, C.K. Aidun, Turbulent channel flow of generalized Newtonian fluids at $Re_\tau = 180$, J. Non-Newton. Fluid Mech. 314 (2023) 105015, https://doi.org/10.1016/j.jnnfm.2023.105015.

[34] A.A. Arosemena, H.I. Andersson, J. Solsvik, Turbulent channel flow of generalized Newtonian fluids at a low Reynolds number, J. Fluid Mech. 908 (2021) A43, https://doi.org/10.1017/jfm.2020.903.

[35] W. Rodi, Experience with two-layer models combining the k-epsilon model with a one-equation model near the wall, in: 29th Aerospace Sciences Meeting, American Institute of Aeronautics and Astronautics, Reston, Virigina, 1991.

[36] H.L. Norris, W.C. Reynolds, Turbulent channel flow with a moving wavy boundary, Ph.D. thesis, Stanford University, California, 1975, https://ui.adsabs.harvard.edu/abs/1975PhDT.....17N.

[37] D.W. Dodge, A.B. Metzner, Turbulent flow of non-Newtonian systems, AIChE J. 5 (2) (1959) 189–204, https://doi.org/10.1002/aic.690050214.

[38] H.R. Anbarlooei, D.O. Cruz, F. Ramos, A.P. Silva Freire, Phenomenological Blasius-type friction equation for turbulent power-law fluid flows, Phys. Rev. E, Stat. Nonlinear Soft Matter Phys. 92 (6) (2015) 5, https://doi.org/10.1103/PhysRevE.92.063006.

[39] A.B. Metzner, J.C. Reed, Flow of non-Newtonian fluids—correlation of the laminar, transition, and turbulent-flow regions, AIChE J. 1 (4) (1955) 434–440, https://doi.org/10.1002/aic.690010409.

[40] L. Eça, F. Pereira, G. Vaz, Viscous flow simulations at high Reynolds numbers without wall functions: is $y^+ \backsimeq$ enough for the near-wall cells?, Comput. Fluids 170 (2018) 157–175, https://doi.org/10.1016/j.compfluid.2018.04.035.

[41] R.M. Clapp, Turbulent heat transfer in pseudoplastic non-Newtonian fluids, in: International Development in Heat Transfer, ASME, vol. Part III, ASME, 1961, pp. 652–661.

[42] D.C. Bogue, A.B. Metzner, Velocity profiles in turbulent pipe flow. Newtonian and non-Newtonian fluids, Ind. Eng. Chem. Fundam. 2 (2) (1963) 143–149, https://doi.org/10.1021/i160006a010.

[43] K.C. Wilson, A.D. Thomas, A new analysis of the turbulent flow of non-Newtonian fluids, Can. J. Chem. Eng. 63 (4) (1985) 539–546, https://doi.org/10.1002/cjce.5450630403.

[44] F. Gori, A. Boghi, A three dimensional exact equation for the turbulent dissipation rate of generalised Newtonian fluids, Int. Commun. Heat Mass Transf. 39 (4) (2012) 477–485, https://doi.org/10.1016/j.icheatmasstransfer.2012.02.010.
[45] P. Csizmadia, C. Hős, Cfd-based estimation and experiments on the loss coefficient for Bingham and power-law fluids through diffusers and elbows, Comput. Fluids 99 (2014) 116–123.
[46] M. Bíbok, P. Csizmadia, S. Till, Experimental and numerical investigation of the loss coefficient of a 90 pipe bend for power-law fluid, Period. Polytech., Chem. Eng. 64 (4) (2020) 469–478.
[47] M. Polizelli, F. Menegalli, V. Telis, J. Telis-Romero, Friction losses in valves and fittings for power-law fluids, Braz. J. Chem. Eng. 20 (2003) 455–463.
[48] R. Cabral, V. Telis, K. Park, J. Telis-Romero, Friction losses in valves and fittings for liquid food products, Food Bioprod. Process. 89 (4) (2011) 375–382.
[49] H. Zhang, T. Xu, X. Zhang, Y. Wang, Y. Wang, X. Liu, Study on local resistance of non-Newtonian power law fluid in elbow pipes, J. Therm. Sci. 25 (3) (2016) 287–291.